

AD-A278 416



ATION PAGE

Form Approved
OMB No. 0704-0188

2

to average 1 hour per response, including the time for reviewing instructions, searching existing data sources, gathering the collection of information. Send comments regarding this burden estimate or any other aspect of this collection of information, including suggestions for reducing this burden, to Washington Headquarters Services, Directorate for Information Operations and Reports, 1215 Jefferson Avenue, Washington, DC 20540, and to the Office of Management and Budget, Paperwork Reduction Project (0704-0188), Washington, DC 20503.

1. AGENCY USE ONLY (Leave blank)		2. REPORT DATE	3. REPORT TYPE AND DATES COVERED FINAL 05 Jul 89 TO 04 Oct 93		
4. TITLE AND SUBTITLE Electrical Characteristics of GaAs MESFET Fabrication by Ion Implantation of Si or Se			5. FUNDING NUMBERS ARPA ORDER NO 6860		
6. AUTHOR(S) Professor T. W. Sigmon			<p style="text-align: center;">DTIC SELECTED APR 20 1994 S B D</p>		
7. PERFORMING ORGANIZATION NAME(S) AND ADDRESS(ES) Department of Electrical Engineering Stanford University Stanford CA 94305-4055					
9. SPONSORING / MONITORING AGENCY NAME(S) AND ADDRESS(ES) AFOSR/NE 110 Duncan Avenue, Suite B115 Bolling AFB Washington DC 20332-0001 Dr. Gerald Witt			8. PERFORMING ORGANIZATION REPORT NUMBER AFOSR OSR-TR- 94 0228		
10. SPONSORING / MONITORING AGENCY REPORT NUMBER F49620-89-C-0094			11. SUPPLEMENTARY NOTES		
12a. DISTRIBUTION / AVAILABILITY STATEMENT APPROVED FOR PUBLIC RELEASE: DISTRIBUTION IS UNLIMITED			12b. DISTRIBUTION CODE		
13. ABSTRACT (Maximum 200 words) <p style="text-align: center;">SEE INTRODUCTION FOR ABSTRACT</p> <p style="text-align: center;">DTIC QUALITY INSURED 3</p>					
14. SUBJECT TERMS			15. NUMBER OF PAGES		
			16. PRICE CODE		
17. SECURITY CLASSIFICATION OF REPORT UNCLASSIFIED			18. SECURITY CLASSIFICATION OF THIS PAGE UNCLASSIFIED	19. SECURITY CLASSIFICATION OF ABSTRACT UNCLASSIFIED	20. LIMITATION OF ABSTRACT UNLIMITED



**SOLID STATE
ELECTRONICS
LABORATORY**

AEOSR-TR- 94 0228

Approved for public release;
distribution unlimited.

**ELECTRICAL CHARACTERISTICS OF GaAs
MESFET FABRICATED BY ION IMPLANTATION
OF SI OR SE**

FINAL REPORT

5 JULY 1989 THROUGH 4 OCTOBER 1993

Contact No. F49620-89-C-0094

Prepared for

Department of the Air Force

Principal Investigator

**T. W. Sigmon
Electrical Engineering**

94-11895



94 4 19 023

Contents

Abstract	iv
1 Introduction	1
1.1 Physical Characteristics of GaAs	1
1.2 Crystal Growth and Processing Techniques	5
1.2.1 Horizontal Bridgman (HB)	5
1.2.2 Liquid Encapsulated Czochralski (LEC)	6
1.3 Epitaxy	7
1.4 Ion Implantation	7
2 Basic Semiconductor Device Physics	10
2.1 Poisson's Equation	11
2.2 Continuity Equations	12
2.3 Current Equations	13
2.4 Summary	14
2.5 Basic Operation of GaAs MESFET	15
2.5.1 Metal Semiconductor Junction	15
2.5.2 Constant Mobility Model of MESFET	18
2.5.3 Numerical Solution of MESFET	21
3 The Properties of EL2	23
3.1 Physical Property	23
3.1.1 The Donor Nature of EL2	23
3.1.2 EL2 as As_{Ga}	24

<input checked="" type="checkbox"/>
<input type="checkbox"/>
<input type="checkbox"/>

Codes

Dist	Avail and/or Special
A-1	

3.1.3	Metestable State of EL2	24
3.2	Theoretical Models of EL2	25
3.2.1	The isolated As_{Ga} model	25
3.2.2	Arsenic Antisite-Arsenic Vacancy ($As_{Ga} - V_{As}$)	25
3.2.3	Arsenic Antisite-Divacancy ($As_{Ga} - V_{Ga} - V_{As}$)	25
3.2.4	Arsenic Antisite-Arsenic Interstitial ($As_{Ga} - As_i$)	26
3.3	The Metastable State EL2*	26
3.4	Optical Mapping of EL2	28
3.4.1	Near-infrared Transmittance Mapping	28
3.4.2	Mapping by Photoluminescence	29
3.5	Effect of EL2 on Device Parameters	30
4	Experimental Setup	31
4.1	Dense Array Pattern Structures	32
4.2	Wafer Processing Conditions	32
4.3	Wafer Testing	37
5	Equilibrium Properties of Pure GaAs	38
5.1	The Thermodynamics of Chemical Reactions	38
5.2	Dilute Solution and Henry's Law	41
5.3	Defect Nomenclature	42
5.4	Native Defects of GaAs	43
5.4.1	Schottky Defects	43
5.4.2	Interstitial Defect	45
5.4.3	Anti-site Defect	45
5.4.4	Frenkel Defect	46
5.4.5	Schottky Anti-site Defect	47
5.4.6	Interstitial Anti-site Defect	47
5.5	Equilibrium Properties of GaAs	47
5.5.1	Pure GaAs	47
5.5.2	GaAs with Carbon and EL2	50

6	Activation Model: Si and Se	52
6.1	Si activation	52
6.2	Se Activation	58
6.3	Discussion	60
7	Short Channel Effects	64
7.1	The Role of Carbon and EL2	64
7.2	Short Channel Effect	68
8	Piezoelectric Effect	73
8.1	Point Force Approximation	73
8.1.1	Stress Distribution	74
8.1.2	Effective Charge Calculation	76
8.2	Gaussian Force Approximation	79
8.3	Discussion	81
9	Conclusions	85
A	Stress Calculation	87
	Bibliography	90

List of Tables

1.1	Physical Properties of GaAs at 300K	4
4.1	Major Structures and Design Rules	32
5.1	Defect Nomenclature	42

List of Figures

1.1	Conventional Unit Cell of GaAs.	2
1.2	The (110) Plane of GaAs.	3
1.3	The (111) Plane of GaAs.	3
1.4	GaAs Growth by Horizontal Bridgeman Method.	5
1.5	LEC growth of GaAs	6
1.6	Molecular Beam Epitaxial of GaAs.	8
2.1	Ideal Metal Semiconductor Junction.	16
2.2	Metal Semiconductor Junction with Large Surface State.	17
2.3	Charge Distribution in Metal Semiconductor Junction.	18
2.4	Schematic of Metal Semiconductor Field Effect Transistor.	19
2.5	Ideal I-V Characteristics of MESFET.	21
4.1	Si profiles calculated for the Lot 1 process using Suprem3.5.	34
4.2	Se profiles calculated for the Lot 1 process from Suprem3.5.	34
4.3	Threshold voltage mapping of a Lot 1 Si implanted wafer.	35
4.4	Threshold voltage mapping for a Lot 1 Se implanted wafer.	36
4.5	Layout for each 3 inch wafer.	37
5.1	Kroger-Vink Diagram of Pure GaAs	51
6.1	Si Activation as a Function of Concentration.	60
6.2	Se Activation as a Function of Concentration.	61
6.3	Fitting of Si Activation to Suprem3.5 Model. The value at the highest dopant density is fitted exactly.	62

6.4	Fitting of Se Activation to Suprem3.5 Model. The value at the highest dopant density is fitted exactly.	62
6.5	EL2 Concentration Resulting From the Fitting of Model Activation to Suprem3.5 Model.	63
7.1	Fermi Level with Respect to the Conduction and Valence Band for Simple PN junction.	65
7.2	Fermi Level with Respect to the Conduction and Valence Band for Junction between n type and semi-insulating region.	66
7.3	Threshold voltage as a function of EL2 concentration. The threshold voltages here is derived from Medici simulation.	67
7.4	Threshold voltage as a function of carbon concentration. The threshold voltages here is derived from Medici simulation.	68
7.5	I-V characteristics of MESFET with and without deep donor EL2 in the substrate.	69
7.6	Vector Diagram of Conduction Current in a MESFET device. EL2 is set at $1 \times 10^{16} \text{ cm}^{-3}$ and Carbon level is at $2 \times 10^{15} \text{ cm}^{-3}$	69
7.7	Vector Diagram of Conduction Current in a MESFET device. Carbon level is at $2 \times 10^{15} \text{ cm}^{-3}$. EL2 is concentration is set to 0.	70
7.8	Threshold voltage as a function of gate length for MESFET devices. Medici simulation shows good agreement with experimental data. . .	71
7.9	Vector diagram of conduction current for short gate MESFET.	71
7.10	Vector diagram of conduction current for long gate MESFET.	72
8.1	Schematic diagram of a GaAs FET used in the calculation of the stress distribution resulting from an opening in dielectric overlayer.	74
8.2	Schematic diagram illustrating the orientation of the coordinate system used in this calculation and that of the MESFETs.	76
8.3	Charge distribution in the channel due to piezoelectric effect. Gaussian force approximation for $1.1 \mu\text{m}$ device, $\sigma = 0.01 \mu\text{m}$	82
8.4	Charge distribution in the channel due to piezoelectric effect. Gaussian force approximation for $1.1 \mu\text{m}$ device, $\sigma = 0.1 \mu\text{m}$	82

8.5	Charge distribution in the channel due to piezoelectric effect. Gaussian force approximation for $5.0\mu\text{m}$ device, $\sigma = 0.1\mu\text{m}$	83
8.6	Piezoelectric shift of the threshold voltage for Si channel implanted devices.	84
8.7	Piezoelectric shift of the threshold voltage for Se channel implanted devices.	84

Chapter 1

Introduction

Since its synthesis in the 1920s by Goldschmidt [1], Gallium Arsenide has received much attention in the last few decades. In the mid-1980s, GaAs technology finally matured into the age of production. We saw a boom of companies dedicated to the growth of GaAs materials and the fabrication of GaAs devices and integrated circuits. Although GaAs is no longer being considered a general purpose material like silicon, it is now well established in several niche markets, such as Direct Broadcast Satellite, Microwave Monolithic Integrated Circuits and Optoelectronics.

1.1 Physical Characteristics of GaAs

Gallium arsenide is composed of the group III element Ga and the group V element As. Each of these two elements form a sublattice of a face-centered-cubic structure. Figure 1.1 shows the Ga and As arrangement in a conventional unit cell. The Ga and As sublattices are offset by $[\frac{1}{4}\frac{1}{4}\frac{1}{4}]$. This crystal configuration is known as cubic sphalerite or zincblende. Therefore, the bond length between nearest neighbors of Ga and As atoms is given by, $r_0 = \sqrt{3}A/4$, where A is the length of the unit cube.

The size of the unit cell for undoped GaAs, both melt-grown and epitaxial at 300K, is given by [2]:

$$A_{300} = 5.65325 \pm 0.00002\text{\AA} \quad (1.1)$$

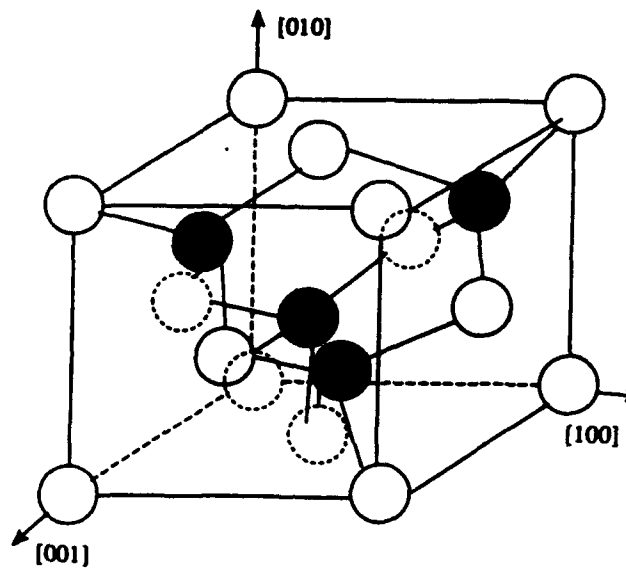


Figure 1.1: Conventional Unit Cell of GaAs.

However, the GaAs lattice constant can increase by up to 0.02% for large concentrations of dopants, such as Sn or Te. In addition, non-stoichiometric GaAs has a slightly smaller value of A for the As-rich crystal and slightly greater A for Ga-rich crystal.

GaAs also has the natural cleavage plane of (110) . Figure 1.2 shows a unit cell bisected by such a plane. This type of plane contains both Ga and As atoms. Another important plane in GaAs is the (111) plane, shown in Figure 1.3. This family of planes only contains one type of atom. As a result, (111) and $(\bar{1}\bar{1}\bar{1})$ planes are not equivalent. Those that only contain Ga atoms are often called $\{111A\}$ and those with only As atoms are called $\{111B\}$. This distinction is important because the different planes have different chemical properties; therefore, have different growth and etching rates. Table 1.1 summarizes the important properties of GaAs at 300K.

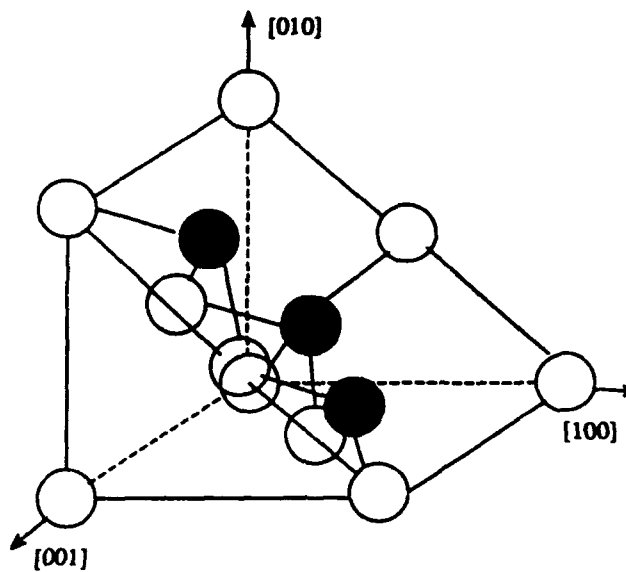


Figure 1.2: The (110) Plane of GaAs.

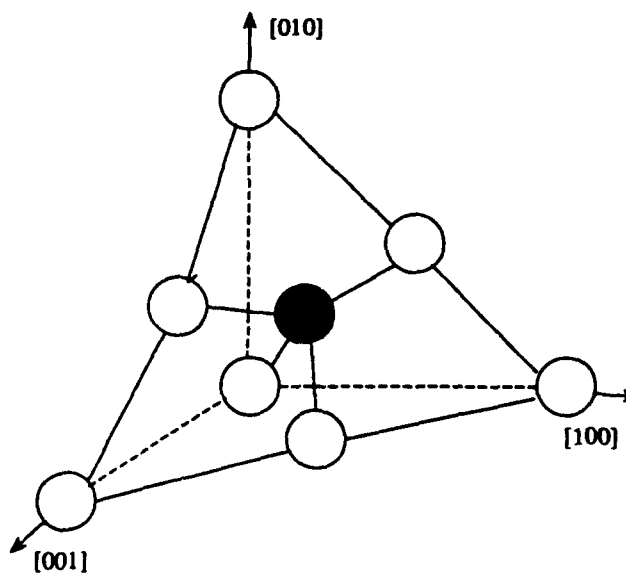


Figure 1.3: The (111) Plane of GaAs.

Molecular Weight (M)	144.6416
Lattice Constant, A	5.65325
Density of Solid, d_s (g cm^{-3})	5.307
Density of Liquid, d_l (g cm^{-3})	5.71
Atomic Concentration, N_a (cm^{-3})	4.42×10^{22}
Melting Temperature, T_m (C)	1238 \rightarrow 1240
Vapor Pressure at T_m , p_m (bar)	0.976
Thermal Diffusivity, D_T (cm^2s^{-1})	0.218
Thermal Conductivity, K ($\text{Wcm}^{-1}\text{K}^{-1}$)	0.49
Linear Expansion Coefficient, α (K^{-1})	5.73×10^{-6}
Specific Heat, ($\text{Jg}^{-1}\text{K}^{-1}$)	0.35
Molar Heat Capacity, C_p ($\text{Jmol}^{-1}\text{K}^{-1}$)	47.026
Standard Enthalpy, H_0 (kJmol^{-1})	-81.643
Standard Entropy, S_0 ($\text{Jmol}^{-1}\text{K}^{-1}$)	64.267
Standard Free Enthalpy, G_0 (kJmol^{-1})	-100.806
Enthalpy for Melting, ΔH_m (kJmol^{-1})	96.7
Stacking Fault Energy, E_{sf} (mJm^{-2})	55.0
Hardness (on Mohs scale)	4 \rightarrow 5
Surface Microhardness (Knoop's Test kgmm^{-2})	750 ± 40

Table 1.1: Physical Properties of GaAs at 300K

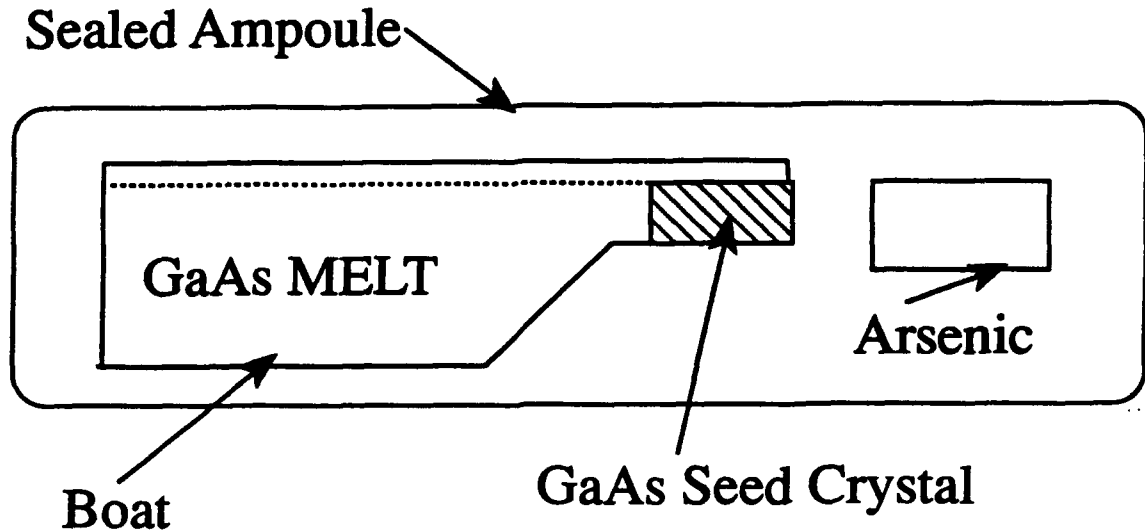


Figure 1.4: GaAs Growth by Horizontal Bridgeman Method.

1.2 Crystal Growth and Processing Techniques

GaAs is grown mainly by two methods, horizontal Bridgman (HB) and Liquid encapsulated Czochralski (LEC). Most commercial wafers today are grown by the later method, although HB grown wafers are still being used in research.

1.2.1 Horizontal Bridgman (HB)

The starting material for the HB method is pure gallium or polycrystalline GaAs, placed in a long boat. The boat is sealed in a quartz ampoule which is typically filled with an inert gas. A GaAs seed crystal is placed in the front of the boat. Elemental arsenic is also present in the ampoule. This configuration is shown in Figure 1.4.

The ampoule is placed in a furnace made up of a number of consecutive heating zones. The temperature along the length of the ampoule is carefully regulated to achieve the desired growth. The elemental arsenic is brought to the gaseous state, while the Ga or poly GaAs is heated to the melting point of GaAs. The temperature

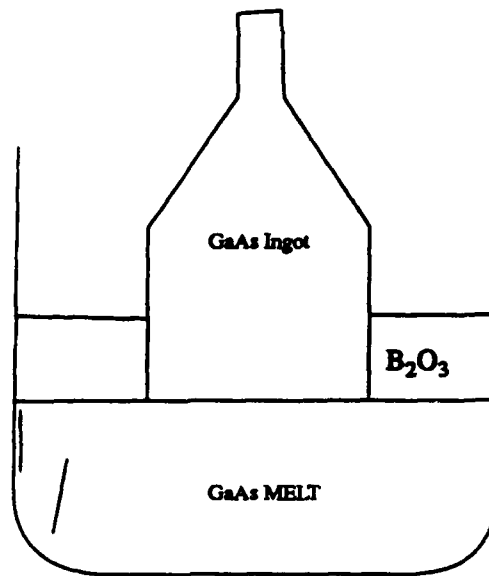


Figure 1.5: LEC growth of GaAs

of the seed region is just below the GaAs solidification point [1]. The crystal is usually grown in the $\langle 111 \rangle$ direction, which is the slow growth direction.

The completed crystal has a shape that matches that of the boat. When (100) oriented wafers are desired, HB crystals are cut at an angle of 54.7° to the ingot axis. By sawing the ingot at an angle, the compositional variations along the axis of the crystal becomes a variation across the wafer; therefore, HB wafers are undesirable for IC type applications.

1.2.2 Liquid Encapsulated Czochralski (LEC)

The starting point for the LEC method is molten GaAs. The melt is confined by a layer of liquid boric oxide (B_2O_3). Both the melt and B_2O_3 are contained in a crucible. Figure 1.5 shows the setup of the LEC method. Crystal growth is started when the GaAs seed penetrates the boric oxide and makes contact with the melt. The diameter of the crystal is controlled by the pull rate [1].

The crucible used in the LEC method is either quartz (SiO_2) or pyrolytic boron

nitride (PBN). The quartz crucible adds Si, which is a n-type dopant, to the grown crystal. In order to maintain the semi-insulating property of the GaAs wafer, Cr, a deep acceptor, is intentionally added. However, Cr doped material has many undesirable effects such as outdiffusion during heating and low distribution coefficient. The use of quartz crucibles is no longer widespread.

GaAs crystal grown with pyrolytic boron crucibles still contain carbon, which comes from the graphite heaters. Carbon is a shallow acceptor and it is compensated by the deep donor EL2 so the material retains the desired semi-insulating property.

1.3 Epitaxy

Epitaxy is the process of growing GaAs material on the surface of a GaAs substrate. Ga and As atoms are brought to the GaAs surface under suitable temperature and concentration. The epitaxial layer of GaAs is typically of much higher quality than the substrate.

In molecular beam epitaxy, the substrate is placed in a vacuum and elemental species are evaporated from ovens and on to the heated substrate. Figure 1.6 illustrates the schematics of a molecular beam epitaxy system. The advantage of MBE is that it can produce almost any epitaxial layer composition, thickness and doping. However, the system requires high vacuum setup as well as other complex and expensive equipment. The growth is also very slow, typically around $1 \mu\text{m}/\text{h}$.

1.4 Ion Implantation

Ion implantation at present is the most economical and widely used method for producing active layers for GaAs FET or MMIC devices. In this process, ions are implanted into the substrate at an energy of 30 to 400 keV at doses of 10^{12} to 10^{14} atoms per cm^2 . The implantation process creates damage to the substrate and the wafers must be subjected to a high temperature annealing step to repair the lattice damage and allow the implanted atoms to move into the proper lattice site. This

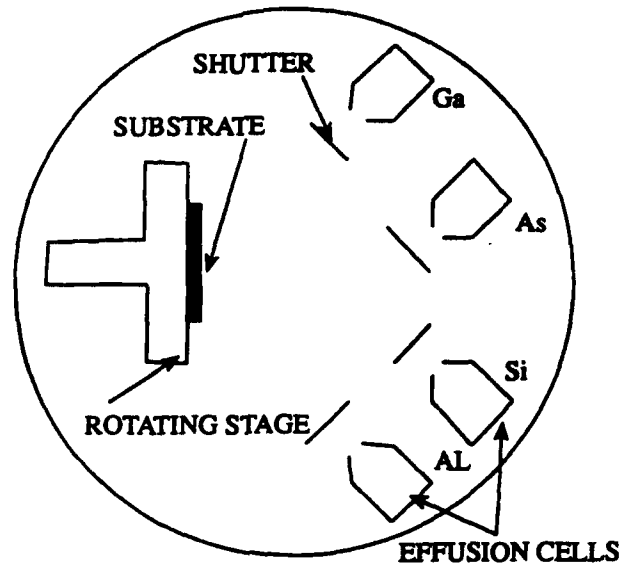


Figure 1.6: Molecular Beam Epitaxial of GaAs.

step is known as activation of the implant. Not all dopants however, become incorporated into a proper lattice site. Therefore, 100% activation is usually achieved, and is typically found to lie in the range of 70% to 90%.

The major advantages and disadvantages of ion implantation are summarized as follows: [3]

- Advantage:

1. Reproducibility, uniformity and high speed of the doping process.
2. Exact control of the amount of dopant.
3. Less stringent requirements on dopant source purity since mass separation is used.
4. Avoidance of high temperature during the implant process itself.
5. Ability to use simple masking methods which allows selective doping.

- Disadvantage:

1. Creation of radiation damage which requires high temperature annealing for repair.
2. Secondary effects, such as diffusion during annealing or channeling during implantation alter the expected dopant profile.

Chapter 2

Basic Semiconductor Device Physics

The set of partial differential equations that govern potential distribution, carrier concentrations and current flow in any semiconductor device are called the basic semiconductor device equations. They may be derived from the Maxwell's equations 2.1 to 2.4.

$$\nabla \times H = J + \frac{\partial D}{\partial t} \quad (2.1)$$

$$\nabla \times E = -\frac{\partial B}{\partial t} \quad (2.2)$$

$$\nabla \cdot D = \rho \quad (2.3)$$

$$\nabla \cdot B = 0 \quad (2.4)$$

where E and D are the electric field and displacement vectors respectively. H and B are the magnetic field and induction vectors. The conduction current density is denoted by J and ρ is the electric charge density.

2.1 Poisson's Equation

To derive Poisson's equation, we need to first introduce a relationship between D and E . This is given by:

$$D = \epsilon E \quad (2.5)$$

where ϵ is the permittivity of the medium. We assume here the permittivity is time independent and spatially homogeneous in the semiconductor. In general, ϵ is represented by a 3×3 matrix. We, however, assume that the material is isotropic and thus ϵ is given by a scalar. For the usual applications in semiconductor devices, these assumptions are quite realistic. For GaAs, $\epsilon = 13.1\epsilon_v$, where ϵ_v is the permittivity constant in vacuum [4].

Due to equation 2.4, we may introduce a vector potential such that:

$$B = \nabla \times A, \quad \nabla \cdot A = 0 \quad (2.6)$$

Substituting equation 2.6 into 2.2, we obtain:

$$\nabla \times \left(E + \frac{\partial A}{\partial t} \right) = 0 \quad (2.7)$$

As a result of equation 2.7, we may introduce the scalar potential ψ as:

$$\nabla \psi = -E - \frac{\partial A}{\partial t} \Rightarrow E = -\frac{\partial A}{\partial t} - \nabla \psi \quad (2.8)$$

We now substitute 2.8 into equation 2.5 and then into 2.1:

$$D = -\epsilon \cdot \frac{\partial A}{\partial t} - \epsilon \cdot \nabla \psi \quad (2.9)$$

$$\nabla \cdot \left(\epsilon \cdot \frac{\partial A}{\partial t} \right) + \nabla \cdot (\epsilon \cdot \nabla \psi) = -\rho \quad (2.10)$$

With a constant permittivity, the first term in the above equation is zero. Thus we

finally arrive at Poisson's equation:

$$\epsilon \nabla^2 \psi = -\rho \quad (2.11)$$

For semiconductor device applications, the space charge density can be further broken down into three parts:

$$\rho = q(p - n + C) \quad (2.12)$$

where p is the concentration of positively charged holes and n is the negatively charged electron density. C represents the ionized dopant profile and is given by the difference between the ionized donor and acceptor profiles.

2.2 Continuity Equations

Applying the divergence operator to the first Maxwell equation 2.1 and using 2.3:

$$0 = \nabla \cdot J + \frac{\partial \rho}{\partial t} \quad (2.13)$$

We now split the conduction into two parts, J_n and J_p , resulting from electrons and holes respectively:

$$J = J_n + J_p \quad (2.14)$$

We also assume that the ionized charge profile is time independent, ie,

$$\frac{\partial C}{\partial t} = 0 \quad (2.15)$$

This effectively neglects contributions from any charged defects, such as vacancies, dislocations and deep recombination traps, which may change their charge state over time.

Then using 2.14, 2.15 and 2.12, we obtain:

$$-\nabla \cdot J_p - q \frac{\partial p}{\partial t} = \nabla \cdot J_n - q \frac{\partial n}{\partial t} \quad (2.16)$$

By setting the left and right side of the above equation equal to qR , we obtain:

$$\nabla \cdot J_n - q \frac{\partial n}{\partial t} = qR \quad (2.17)$$

$$\nabla \cdot J_p + q \frac{\partial p}{\partial t} = -qR \quad (2.18)$$

Obviously, we can not gain any additional information by splitting a single equation into two equations. However, these formal steps can help us interpret the equations more easily. The quantity R may be understood as the difference of the rate at which electron and hole carriers pairs recombine and the rate at which they are generated in the semiconductor. Therefore, we call R the recombination-generation rate. Positive R would mean net recombination and negative R means net generation. However, if R is modeled with the knowledge of solid state and statistical physics, each of these two equations has a meaning of its own and should be considered as two equations.

2.3 Current Equations

We assume here there are two types of current in the semiconductor device. The diffusion of the electron and hole ensembles results in diffusion current J_n^{diff} , J_p^{diff} and the drift of electrons and holes caused by the electric field results in drift current J_n^{drift} , J_p^{drift} . We also assume that the total current is determined by linearly superimposing the diffusion and drift currents:

$$J_n = J_n^{diff} + J_n^{drift}, \quad J_p = J_p^{diff} + J_p^{drift} \quad (2.19)$$

Electron and holes diffuse from regions of high respective concentrations to regions of lower concentrations. The direction of such diffusion is the direction of steepest descent of particle concentration. Therefore, the diffusion flux densities must be proportional to the gradients of the particle concentration. As a result, the diffusion currents are given by:

$$J_n^{diff} = qD_n \nabla n \quad (2.20)$$

$$J_p^{diff} = -qD_p \nabla p \quad (2.21)$$

The signs are chosen here so that the diffusion coefficients D_n and D_p are positive. The drift currents are given by:

$$J_n^{drift} = qn v_n^d \quad (2.22)$$

$$J_p^{drift} = qp v_p^d \quad (2.23)$$

where v_n^d and v_p^d are the average drift velocity of electrons and holes respectively. The drift of holes has the same orientation as the electric field while the drift of electrons has the opposite direction. The drift velocities are related to the electric field by:

$$v_n^d = -\mu_n E, \quad v_p^d = \mu_p E \quad (2.24)$$

where μ_n and μ_p are the electron and hole mobilities. By inserting equations 2.22, 2.23 and 2.24 into 2.19, we obtain the current relations:

$$J_n = qD_n \nabla n + q\mu_n n E \quad (2.25)$$

$$J_p = -qD_p \nabla p + q\mu_p p E \quad (2.26)$$

Clearly, the above equations are derived from a phenomenological approach instead of well established physical principles. Therefore, the current equations are not to be accepted in the same way as Poisson's equation and the continuity equations. Their validity must be investigated by other means. A more rigorous approach to the derivation of the current equations leads to the same expressions by starting with the Boltzman transport equation [7].

2.4 Summary

The basic semiconductor device equations are given as:

$$\text{Poisson's Equation} \quad \epsilon \nabla^2 \psi = q(n - p - C) \quad (2.27)$$

$$\text{Electron Continuity } \nabla \cdot J_n - q \frac{\partial n}{\partial t} = qR \quad (2.28)$$

$$\text{Hole Continuity } \nabla \cdot J_p + q \frac{\partial p}{\partial t} = -qR \quad (2.29)$$

$$\text{Electron Current } J_n = q\mu_n n E + qD_n \nabla n \quad (2.30)$$

$$\text{Hole Current } J_p = q\mu_p p E - qD_p \nabla p \quad (2.31)$$

2.5 Basic Operation of GaAs MEFSET

Unlike Si, GaAs does not have a native oxide, so devices such as the Metal Oxide Silicon Field Effect Transistor (MOSFET) can not be fabricated. The most dominant device in both digital and analog applications is the Metal Semiconductor Field Effect Transistor (MESFET). It closely resembles a Junction Field Effect Transistor (JFET) but uses a metal gate to control the current transport in the channel by modulating the extent of the depletion region formed by the Schottky barrier.

2.5.1 Metal Semiconductor Junction

When a metal and a semiconductor are brought into intimate contact, electron transfer will take place between the systems. When equilibrium is reached, every process and its reverse is occurring at the same rate and no net electron transfer occurs. The two system will thus have the same Fermi energy.

Let's define the work function as the energy difference between the Fermi and the vacuum levels. Let $q\phi_m$ be the work function of the metal and $q(\chi + V_n)$ be the work function for the semiconductor. Here χ is the electron affinity measured from the conduction band E_c to the vacuum level and V_n is the energy difference between E_c and Fermi level. These definitions are illustrated in Figure 2.1.

As the contact is formed, electrons at the Fermi level in the metal see a barrier of $q\phi_{Bn}$ and the electrons at the conduction band edge in the semiconductor see a barrier height of qV_{Bi} . In equilibrium, we have [6]:

$$q\phi_{Bn} = q(\phi_m - \chi) \quad (2.32)$$

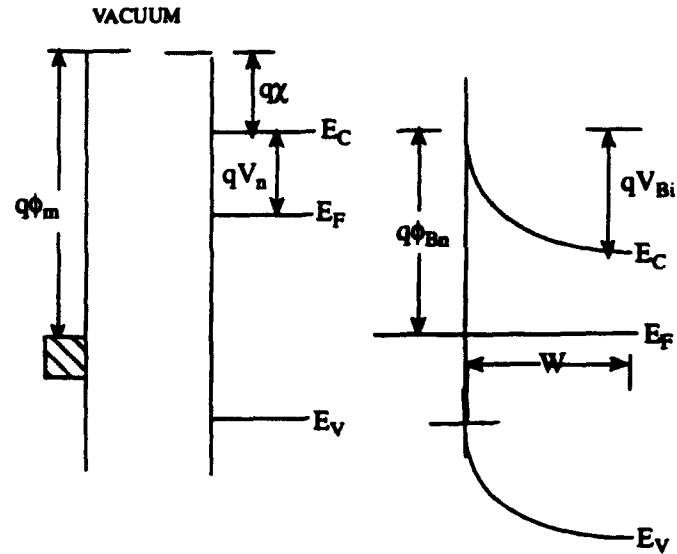


Figure 2.1: Ideal Metal Semiconductor Junction.

$$qV_{Bi} = q(\phi_m - \chi) - qV_n \quad (2.33)$$

The above equations only hold if there are no surface states. Usually, however, semiconductors have significant amount of surface states which often lie in the bandgap. Therefore, real metal semiconductor junctions are never quite in accord with the above model. Si comes very close to the ideal situation, but most compound semiconductors do not [7].

In the case of large numbers of surface states, as shown in Figure 2.2, all the electron transfer required to achieve equilibrium can be accommodated at the surface. Therefore, space charge in the semiconductor remains unaffected. As a result, the barrier height is determined by the properties of the semiconductor alone and is independent of the metal. This case applies to semi-insulating GaAs and the experimentally measured barrier height is found to be 0.78 eV.

The charge distribution diagram for an ideal metal semiconductor junction is shown in Figure 2.3. Since metal closely approximates a perfect conductor, the charge transferred to it from the semiconductor exists only on the surface in a thin plane. In

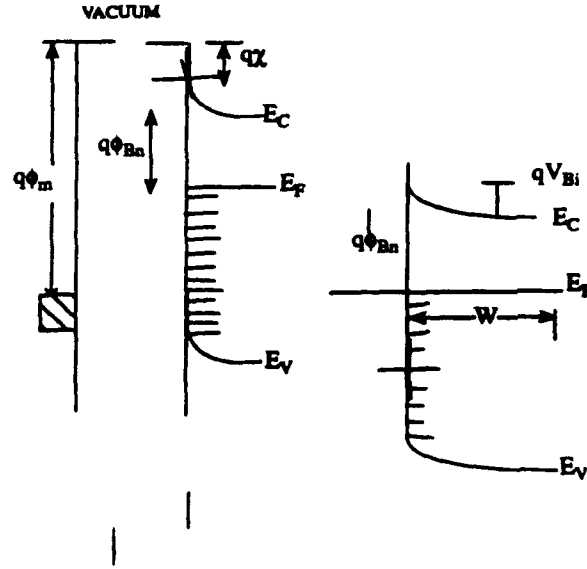


Figure 2.2: Metal Semiconductor Junction with Large Surface State.

the n- type semiconductor, the charge consists of ionized donors, electrons and holes. The hole concentration is extremely small since it's the minority carrier. Under the depletion approximation, we also assume that the electron concentration in the depletion region which extends to $x=x_d$ is much less than the ionized donor concentration. Outside of the depletion region, the electron and ionized donor densities are assumed to be equal.

Under the depletion approximation, the Poisson's equation may be transformed as:

$$-\frac{\partial^2 V}{\partial x^2} = \frac{\partial \mathcal{E}}{\partial x} = \frac{q}{\epsilon} (p(x) - n(x) + N_D^+(x) - N_A^-(x)) \quad (2.34)$$

$$-\frac{\partial^2 V}{\partial x^2} \approx \frac{q}{\epsilon} N_D \quad \text{for } 0 < x \leq x_d \quad (2.35)$$

The electric field \mathcal{E} can then be solved for as:

$$\mathcal{E}(x) = \mathcal{E}_m - \frac{qN_D x}{\epsilon_s} = \frac{qN_D}{\epsilon_s} (x_d - x) \quad (2.36)$$

where \mathcal{E}_m is the maximum field that exists at $x=0$. The potential may be obtained

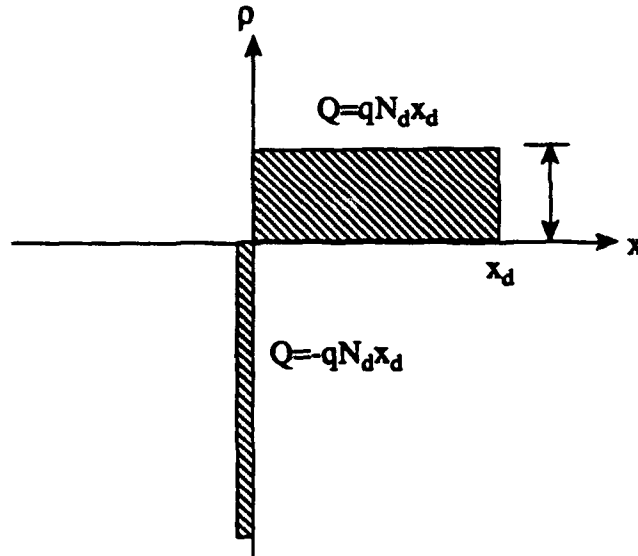


Figure 2.3: Charge Distribution in Metal Semiconductor Junction.

by integrating the electric field equation.

$$V(x) = \frac{qN_D}{\epsilon_s} \left(x_d x - \frac{1}{2} x^2 \right) + \phi_B \quad (2.37)$$

The depletion width may be obtained by setting $x = x_d$ in the above equation where the potential is equal to V_n and $V_{bi} = \phi_B - V_n$. So we obtain:

$$x_d = \left(\frac{2\epsilon}{qN_d} (V_{bi} - V) \right)^{\frac{1}{2}} \quad (2.38)$$

where V is the applied potential.

2.5.2 Constant Mobility Model of MESFET

The assumption of constant mobility is accurate in the case of long gate-length FET where the field is sufficiently small. Figure 2.4 illustrates the geometry of such a device. The source here is grounded and drain biased to a small positive voltage.

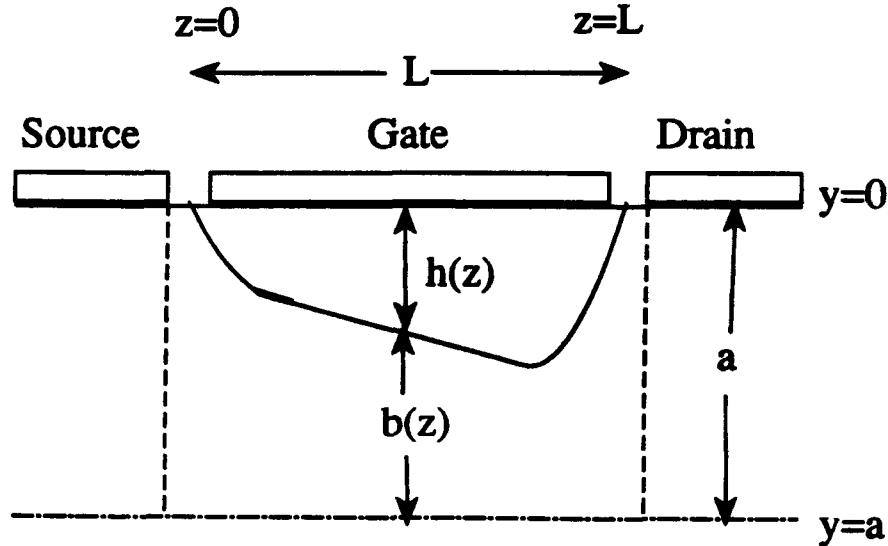


Figure 2.4: Schematic of Metal Semiconductor Field Effect Transistor.

The gate is negatively biased and the absolute value of the gate bias is V_G . Then, the depletion layer width $h(z)$ varies slowly along the channel. The electric field in the depletion region is along the y axis and in the channel region is along the z axis [7].

The depletion width $h(z)$ at any region along the channel is inferred from equation 2.38:

$$h(z) = \left(\frac{2\epsilon[V(z) + V_G + V_{bi}]}{qN_D} \right)^{\frac{1}{2}} \quad (2.39)$$

where $V(z)$ is the channel potential at point z arising from the finite drain bias. So at the source end, we have:

$$h(z = 0) = \left[\frac{2\epsilon(V_G + V_{bi})}{qN_D} \right]^{\frac{1}{2}} \quad (2.40)$$

$$h(z = L) = \left[\frac{2\epsilon(V_G + V_G + V_{bi})}{qN_D} \right]^{\frac{1}{2}} \quad (2.41)$$

At $h(z=L)=a$, the channel is pinched off and saturation of the current occurs. Therefore, the pinch-off voltage is given by:

$$V_p = \frac{qN_D a^2}{2\epsilon} \quad (2.42)$$

This is the voltage needed between gate and drain to result in saturation of the current. It is also the voltage between gate and source to shut off the current since we achieve complete channel depletion at that voltage. The threshold voltage is therefore defined as:

$$V_{th} = V_p - V_{bi} \quad (2.43)$$

Since the field is small in this approximation, there is only a small deviation to quasi-neutrality and thus only small gradient in carrier concentration. To the first-order approximation, we may neglect any diffusion current. So:

$$I_D = qN_D \mu W [a - h(z)] \frac{dV}{dz} \quad (2.44)$$

where W is the width of the device. By squaring the equation for $h(z)$ and differentiating it, we obtain:

$$2h dh = \frac{2\epsilon}{qN_D} dV \quad (2.45)$$

and therefore

$$I_D = W q N_D \mu (a - h) \frac{q N_D}{\epsilon} h \frac{dh}{dz} \quad (2.46)$$

By applying the current continuity condition and integrating over the above equation, we obtain;

$$\int_0^L I_D dz = \frac{(qN_D)^2 \mu W}{\epsilon} \int_{h(0)}^{h(L)} (a - h) h dh \quad (2.47)$$

$$I_D = \frac{W \mu q^2 N_D^2 a^3}{6\epsilon L} \left\{ \frac{3}{a^2} [h^2(L) - h^2(0)] - \frac{2}{a^3} [h^3(L) - h^3(0)] \right\} \quad (2.48)$$

Figure 2.5 shows an ideal I-V characteristic for the MESFET. The current is saturated when the gate to source voltage reaches V_p .

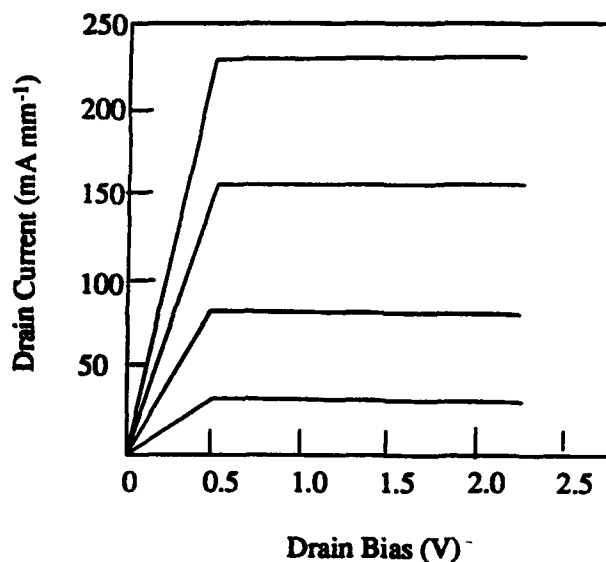


Figure 2.5: Ideal I-V Characteristics of MESFET.

2.5.3 Numerical Solution of MESFET

In order to obtain an accurate solution for the electrical characteristics of the MESFET that is applicable to short channel devices, which are most often used in actual applications, we must solve the set of basic semiconductor device equations numerically along with suitable boundary conditions.

Let's write the potential Ψ in the Poisson's equation as the intrinsic Fermi level. Then [5]:

$$-q\Psi = E_c - \frac{E_g}{2} + \frac{kT}{2} \ln \frac{N_v}{N_c} \quad (2.49)$$

As a result, the boundary conditions at the source and drain region, which are ohmic are:

$$n = \frac{1}{2}[(N_d^+ - N_a^-) + \sqrt{(N_d^+ - N_a^-)^2 + 4n_i^2}] \quad (2.50)$$

$$\Psi = V_a + \frac{kT}{q} \ln \frac{n}{n_i} \quad (2.51)$$

where V_a is the applied voltage.

For the Schottky gate contacts, we have the following relations:

$$\Psi = \chi + \frac{E_g}{2q} + \frac{kT}{2q} \ln \frac{N_c}{N_v} - \phi_m + V_a \quad (2.52)$$

$$\vec{J}_n \cdot \vec{n} = -qv_n \left(n - \frac{\sqrt{C^2 + 4n_i^2} + C}{2} \right) \quad (2.53)$$

where ϕ_m is the metal work function, χ the electron affinity of the semiconductor and v_n the surface recombination velocity.

For regions interfacing with insulators, the potential and electron concentration must obey the following relationships at the boundary.

$$\frac{\partial \Psi}{\partial \vec{n}} = 0 \quad \vec{J}_n \cdot \vec{n} = 0 \quad (2.54)$$

These boundary conditions plus the basic set of semiconductor device equations are implemented in Pisces [8], a device simulation program. This program is further refined in a commercial program called Medici [9]. This is the program that we shall use to model our MESFETs.

Chapter 3

The Properties of EL2

The native defect EL2 in semi-insulating GaAs crystals grown by the liquid encapsulated Czochralski (LEC) method has been the subject of intensive research in recent years. This defect, which is associated with the As antisite (As_{Ga}) and is responsible for semi-insulating behavior, also plays an important role in affecting GaAs MES-FET device parameters. As we will see later, any variation in the concentration of EL2 will effect the uniformity of electrical parameters of devices fabricated by direct ion implantation into semi-insulating substrates. This in turn will effect the realization of high performance GaAs LSI circuits. Despite an intensive research effort to understand the nature of EL2, much controversy still remains.

3.1 Physical Property

3.1.1 The Donor Nature of EL2

The donor nature of EL2 was clearly demonstrated by Mircea et al. [10] Their experiment consisted of studying EL2 outdiffusion after a 600-750°C annealing in VPE materials. The experiment clearly established that EL2 centers are electrically neutral when occupied by electrons and are positively charged when these electrons are released.

From the thermal electron emission rate and electron capture cross section one

can obtain the free energy of ionization, E_T with respect to the conduction band minimum as: [11]

$$E_T = (0.730 \pm 0.02) - \frac{\alpha T^2}{T + 204} \quad (3.1)$$

where $\alpha = (3.5 \pm 0.6) \times 10^{-4} \text{eVK}^{-1}$.

3.1.2 EL2 as As_{Ga}

EL2 is thought to be a native defect which contains an arsenic antisite (As_{Ga}) at least as part of its physical structure. This has been established by stoichiometry studies [12] and electron paramagnetic resonance data [13]. To establish the connection between EL2 and As_{Ga} , one can compare the spectroscopic data for EL2 and As_{Ga} . The comparison is complicated by the fact that EL2 was originally detected and defined by electrical techniques, while As_{Ga} was studied by magnetic resonance. Fortunately, when suitably combined with optical methods, both techniques provide information about the optical properties of the respective species. This optical connection is considered to be the key to associating EL2 with As_{Ga} .

3.1.3 Metestable State of EL2

The EL2 defect possesses both normal and metastable states ($EL2^*$). The transformation from normal to metastable states can be achieved by illumination of 1.1eV energy monochromatic light at low temperature. The metastable state can be brought back to the normal state by heating the sample above 120K. The $EL2^* \rightarrow EL2$ transformation is believed to occur through the neutral state $EL2^0$ with a much higher probability than the charged state $(EL2)^+$ [14]. The configuration of $EL2^*$ remains unknown since no electrical or optical properties of this state has yet been discovered.

3.2 Theoretical Models of EL2

3.2.1 The isolated As_{Ga} model

The isolated As_{Ga} model is the simplest physical model since the correlation of EL2 with As_{Ga} . The main concern of supporters of this theory has been the search for large lattice relaxations. Since Bachelet and Scheffler [15] proposed that relaxations associated with the isolated As_{Ga} defect cannot introduce a LLR, which is believed necessary to account for the metastable state of EL2.

It was finally shown that metastability could also arise from the isolated As_{Ga} defect when it underwent a symmetry breaking distortion. By using the self-consistent Green's function method, the metastable state is called the M configuration and identified as a gallium vacancy plus an arsenic interstitial ($V_{Ga} - As_i$) pair defect. However, many recent experiments, such as neutron irradiation show that EL2 is a more complex defect than a simple point defect [14].

3.2.2 Arsenic Antisite-Arsenic Vacancy ($As_{Ga} - V_{As}$)

This model was theoretically studied by a Green's function method. It was found that V_{Ga} is a multiple acceptor which can be either neutral or negatively charged. The $As_{Ga} - V_{As}$ is formed by the probable atomic motion occurring during annealing of a crystal, which causes one of the four nearest neighbor arsenic atoms to fill the gallium vacancy.

This model also satisfies the metastability property of EL2, but conflicts with the electron paramagnetic resonance data (EPR). However, EPR measurements were performed only on electron irradiated materials and a definitive conclusion requires additional experiments.

3.2.3 Arsenic Antisite-Divacancy ($As_{Ga} - V_{Ga} - V_{As}$)

According to this model, the EL2 configuration is formed by a $V_{Ga} - V_{As}$ on second and third neighbor positions with respect to As_{Ga} . The EL2* configuration corresponds to an As_{Ga} separating the two vacancies.

Detailed calculations have not as yet been made for this model; however, the latest interpretation of the EL2 EPR spectrum supports the $As_{Ga} - V_{Ga} - V_{As}$ model. In addition, recent thermal annealing measurements also support this three point defect model.

3.2.4 Arsenic Antisite-Arsenic Interstitial ($As_{Ga} - As_i$)

In this model, the stable and metastable atomic configurations of EL2 are explained as As_i in the second and first nearest neighbor positions, respectively. Self-consistent Green's function techniques are carried out to calculate the electronic structure and binding energy of the model. It is found that in order to identify EL2 with this model, the As_i atom has to be positively charged, that is the defect state has to be $As_{Ga} - As_i^+$. This finding requires that an acceptor level be present to account for the compensation mechanism. This acceptor level has not as yet been identified. However, the $As_{Ga} - As_i$ model is supported by EPR and deep-level transient spectroscopy data. In addition, optically detected electron nuclear double resonance (ODENDOR) experiments on semi-insulating GaAs material also finds a second defect near As_{Ga} , which is identified as the arsenic interstitial [14].

3.3 The Metastable State EL2*

The understanding of EL2* is one of the keys to understanding the nature of EL2, unfortunately, when the stable state is transformed into the metastable state, its normal optical and electrical properties are quenched out and the state becomes virtually inaccessible experimentally. As a result, very little is known about EL2*.

Since no electrical or optical properties are known about EL2*, studies of EL2* are concentrated on the recovery to the stable state, $EL2^* \rightarrow EL2$. It is known that the recovery of EL2* can be achieved by heating the sample to about 120K or higher for a short period of time. The activation energy for this thermal process has been measured by various workers and their values vary from about 0.25 to 0.36 eV. This indicates the possibility of sample dependent activation energy, which is confirmed by

further experiments. This indicates that the metastable state does not have a unique structure and lends support to the concept of the "EL2 family" of defects.

The lack of any known electrical or optical properties has led to the proposal that EL2* is electrically and optically inactive. A direct consequence of non-electrical activity is that EL2 dominated semi-insulating GaAs should become p-typed after EL2 is transformed into its metastable state.

As we know that the semi-insulating behavior of GaAs is produced by compensation of a residual shallow acceptor by the deep level EL2, effectively pinning the Fermi level near mid gap which produces high resistivity. If EL2 is rendered electrically inactive, then the electrical properties of the material should be dominated by the shallow acceptors. This means that a thermal current should be detectable for all temperatures above 8K until EL2 recovers from the metastable state.

Experiments were performed by Jimenez [16] in accordance with this theory. He observed a persistent photocurrent (PPC). However the author stated that the PPC effect was not universally observed and only observed for certain samples. In addition, the reported hole concentration of $4 \times 10^9 \text{ cm}^{-3}$ is too low to be thermally ionized carbon at their experimental temperature of 77K.

A survey of remainder of the literature on this subject indicates that the occurrence of the PPC is an exception rather than the rule as required by the non-electrical activity hypothesis of EL2. The question naturally arises that if there is not any PPC after quenching of EL2, the acceptors must be compensated by a donor state. The simplest answer is to assume that EL2* is responsible for such compensation. Calculations of electronic properties of the $As_{Ga} - As_i$ model and isolated As_{Ga} model shows such possibilities do exist; however, further calculations are needed to give a definitive answer.

3.4 Optical Mapping of EL2

3.4.1 Near-infrared Transmittance Mapping

For a wafer of uniform thickness t with polished planar faces, the reflection coefficient for a paraxial incident flux of light, using focusing lens of large f number is:

$$R = \frac{(n - 1)^2}{(n + 1)^2} \quad (3.2)$$

where n is the refractive index and is fitted to experimental data at room temperature as: [17]

$$n_{300}(h\nu) = \{7.10 + 3.78[1 - 0.180(h\nu)^2]^{-1}\}^{1/2} \quad (3.3)$$

Let the paraxial incident photon flux be I_0 and flux emerging from the far side of the wafer be I_T , then the fractional transmittance can be shown to be:

$$T \equiv \frac{I_T}{I_0} = (1 - R)^2 \exp(-\alpha t) [1 - R^2 \exp(-2\alpha t)]^{-1} \quad (3.4)$$

where α is the optical absorption coefficient and can be solved for as:

$$\exp(\alpha t) = \frac{(1 - R)^2}{2T} \{1 + [1 + 4R^2 T^2 (1 - R)^{-4}]^{1/2}\} \quad (3.5)$$

Using the above equations, for a sample of known thickness t and a selected $h\nu$, the measured value of T will immediately yield a value for α .

For undoped GaAs containing EL2 at a concentration N^0 in the neutral state and N^+ in the ionized state, the total absorption coefficient for near IR extrinsic $h\nu$ can be expressed as:

$$\nu = \sigma_n^0 N^0 + \sigma_p^0 N^+ + \alpha_0 \quad (3.6)$$

where σ_n^0 is the optical absorption cross section for neutral EL2 sites, measured by photocapacitance methods by Chantre et al [18], σ_p^0 is the hole photoionization cross sections, measured by P. Silverberg, et al [19]. The final term α_0 lumps together any

absorption processes unrelated to EL2, which must be quite small at room temperature, at which the experiments are performed. EL2 mapping experiments such as this has been conducted by P. Dobrilla, et al. [17, 20].

3.4.2 Mapping by Photoluminescence

The results obtained using the near-IR transmittance method have a limited spatial resolution on the order of the thickness of the wafer. Furthermore, they are the average value over the thickness of the wafer, and may or may not reflect the surface device active area of the wafer. This shortcoming is overcome by using the Photoluminescence (PL) method.

When light of photon energy larger than the band gap is incident on the surface of the wafer, excess carriers are created in the conduction and valence bands. Carriers of one type can recombine directly with those of the other type, or be trapped first by a deep level and then recombine. PL occurs as a result of the radiative recombination process.

Let's assume that the carrier lifetime (τ) is limited by recombination via "lifetime-killer" centers, and the concentration of excited carriers (n_{ex}) is larger than the intrinsic carrier concentration and the concentration of the deep levels N_D . The intensity of the band-to-band transition (I_B) and that of the deep level (I_D) are [21]:

$$I_B \propto n_{ex}^2 \tau \quad (3.7)$$

$$I_D \propto n_{ex} \tau N_D \quad (3.8)$$

Therefore, under a constant excitation condition, I_B is proportional to τ , or inversely proportional to the concentration of the "killer centers." This implied that the spatial variation of I_B reflects the spatial inhomogeneity of the crystalline quality. The intensity I_D , on the other hand, is proportional to τN_D . Assuming that the variation of τ on a wafer is small, then the variation of I_D reflects the distribution of the deep levels.

Such PL experiments were conducted by Tajima [22]. The measurement was

carried out at room temperature in air. The sample was mounted on an X-Y stage with a travel distance of 100 mm for both axes. The diameter of the laser beam varied from 0.1 to 1 mm with an incident power of 0.1 to 100 W cm⁻². The PL signal is analyzed with an apparatus of high optical efficiency, consisting of a grating monochromator with a 75 and a 600 grooves/mm grating blazed at 2.0 and 1.0 μm, respectively, and Ge and PbS detectors. A deep level PL band with a peak of 0.65 eV was observed and is believed to be traceable to EL2.

3.5 Effect of EL2 on Device Parameters

The effect of dislocations and EL2 on the electrical properties of devices have been widely studied and debated. Although EL2 as a donor is electrically inactive in the n channel FET fabricated by direct ion implantation, it can well affect the activation ratio of the implants, especially the amphoteric Si implant, thus affecting the device parameters. Studies performed by Dobrilla and Blakemore [23] show that a large value of N^0 , the neutral EL2 concentration, tends to make I_{dss} larger and V_{th} more negative. Their experiments are done using near-IR transmittance mapping of EL2 and KOH etching to reveal dislocation etch pits following various electrical measurements. They report that one of their wafers had a uniform dislocation density as revealed by KOH etching and a radially symmetrical N^0 distribution. They were able to correlate the device parameters with EL2 density for this particular wafer.

However, studies done by Miyazawa and Wada [24] found evidence for the influence of dislocation proximity to a device on threshold voltage. They found an increase of $5 \pm 2mV$ in V_{th} per 1 μm, for a gate to pit distance below about 50 μm. It was also found that EL2 and dislocations are correlated [25]. The results by Miyazawa and Blakemore do not in fact contradict each other.

Chapter 4

Experimental Setup

We have taken an extremely versatile approach to focus on the study of issues effecting GaAs MESFET electrical characteristics. Our purpose is to develop and substantiate, through experimental design, fabrication and testing, models for understanding of the relationships between material and process defects, or variations, on the performance and uniformity of GaAs digital ICs. Our approach is to couple the modeling and design effort with an advanced manufacturing facility to allow controlled, state-of-art device fabrication processes to be used to test the models being developed and to assist in the design of realistic test structures. Therefore, a unique part of this effort is the cooperative design of test structures specifically aimed at substrate material defects and ion implantation process variations using a state-of-art sub-micron MESFET foundry process. Further test structures, aimed at such important topics as device scaling and gate orientation, are also included. These test structures, are part of a reticule which is stepped over the entire wafer to minimize the effects of lithographic misalignment. Computer automated testing of the test structures allows extension of the modeling effort to wafer scale, which due to the inherent foundry process control, allows the eventual prediction of wafer yields resulting from spatially dependent defects and processes, such as dislocations and ion implantation.

Table 4.1: Major Structures and Design Rules

Major Structures	Design Rule
FET Array	Size $1\mu \times 1\mu$, gate to gate spacing $11.5\mu m$. E-D cell spacing $22.5\mu m$
D-mode, E-mode	Gate length: 0.5, 1.2, 2.0, 5.0, 8.0 μm . Width: 2, 10, 20 and 50 μm

4.1 Dense Array Pattern Structures

The Advanced Test Structure mask set was designed for use with the state-of-the-art, self-aligned, refractory gate MESFET process available at the Rockwell foundry. The test structures utilize fabrication technology capable of producing both enhancement (E) and depletion (D) mode MESFET devices on the same wafer. We however utilize this technology to implant different ion species into the channel of MESFETs in close proximity. This allows a direct comparison of the effects of different ion species under similar conditions. This approach eliminates complications caused by spatially or wafer dependent defect structures or background acceptor concentrations.

Table 4.1 identifies the various structures available on the ATS for testing. As seen in this table, the ATS contains channel implants of Si and Se dopants in FETs in close proximity. FETs with different gate lengths and gate widths are also fabricated for examination of short channel and backgating effects. Gate lengths include 0.5, 0.6, 0.7, 0.8, 0.9, 1.0, 1.1, 1.2, 2, 5 and 8 μm .

4.2 Wafer Processing Conditions

The following list outlines the fabrication process for what we shall refer to as Lot 1 wafers. There are a total of fourteen (100) oriented wafers taken from the same boule, processed in this Lot.

- n^- channel implants.

1. Se: Energy=124 KeV, Dose= $3.33E12\text{ cm}^{-2}$.

2. Si³¹: Energy=50 KeV, Dose=4.75E12 cm^{-2} .
 3. SiF: Energy=85 KeV, Dose=4.75E12 cm^{-2} .
- Anneal: Temperature=850°C, Time=20 minutes.
 - Gate Lithiography.
 - LDD nitride deposition.
 - n^+ implant of SiF, Energy=150 KeV, Dose=2.2E13 cm^{-2} .
 - Anneal: Temperature=790°C, Time=20 minutes.
 - isolation implant.
 - ohmic lithiography.
 - alloying.
 - nitride deposition.
 - via definition.
 - metal 1.

Figures 4.1 and 4.2 show the dopant profiles of Lot 1 process. These profiles are obtained from the Stanford GaAs process simulator, Suprem3.5 [37].

For Lot 2, we repeat the Lot 1 process except that wafers from three different vendors are used. Since the absolute value of the threshold voltage for the Se channel implanted devices in Lot 1 was found experimentally to be below target, we increased the Se implant dose from $3.33 \times 10^{12} cm^{-2}$ to $4.00 \times 10^{12} cm^{-2}$ for this Lot.

Figure 4.3 and 4.4 show the threshold voltage maps across two wafers. We notice that there is quite a bit of threshold voltage variation across the wafers.

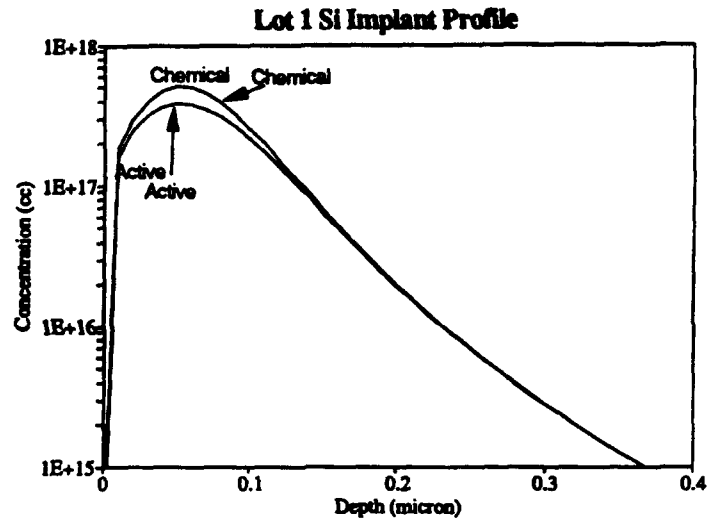


Figure 4.1: Si profiles calculated for the Lot 1 process using Suprem3.5.

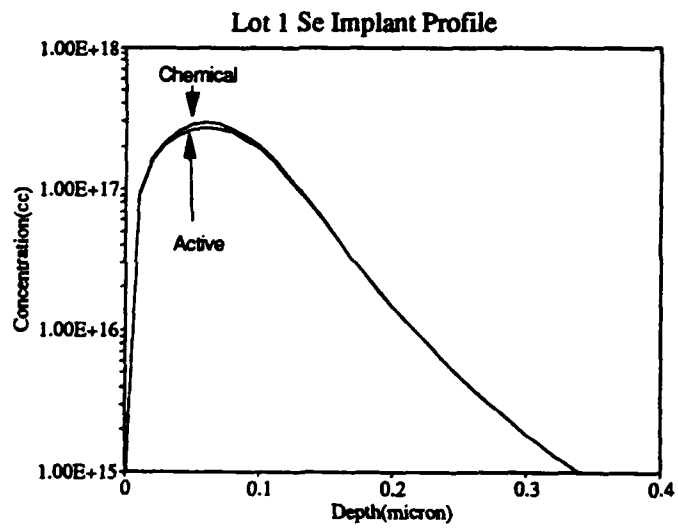
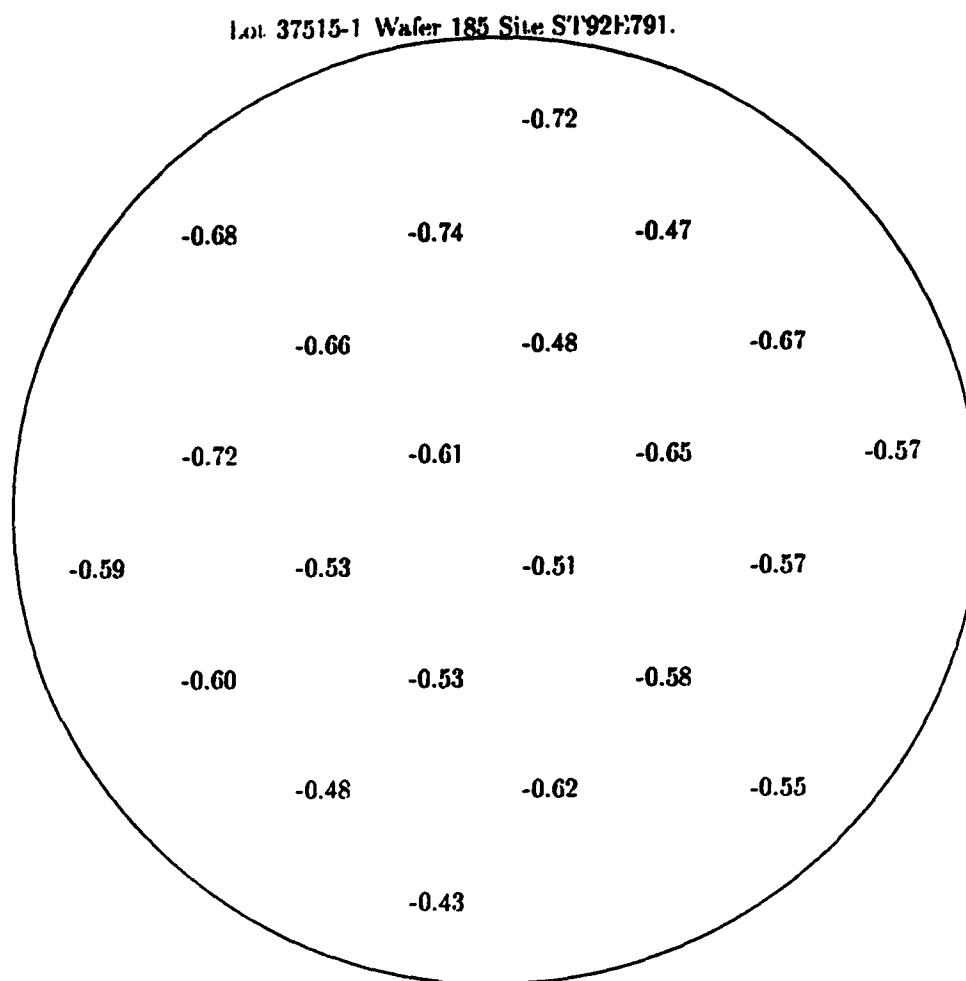
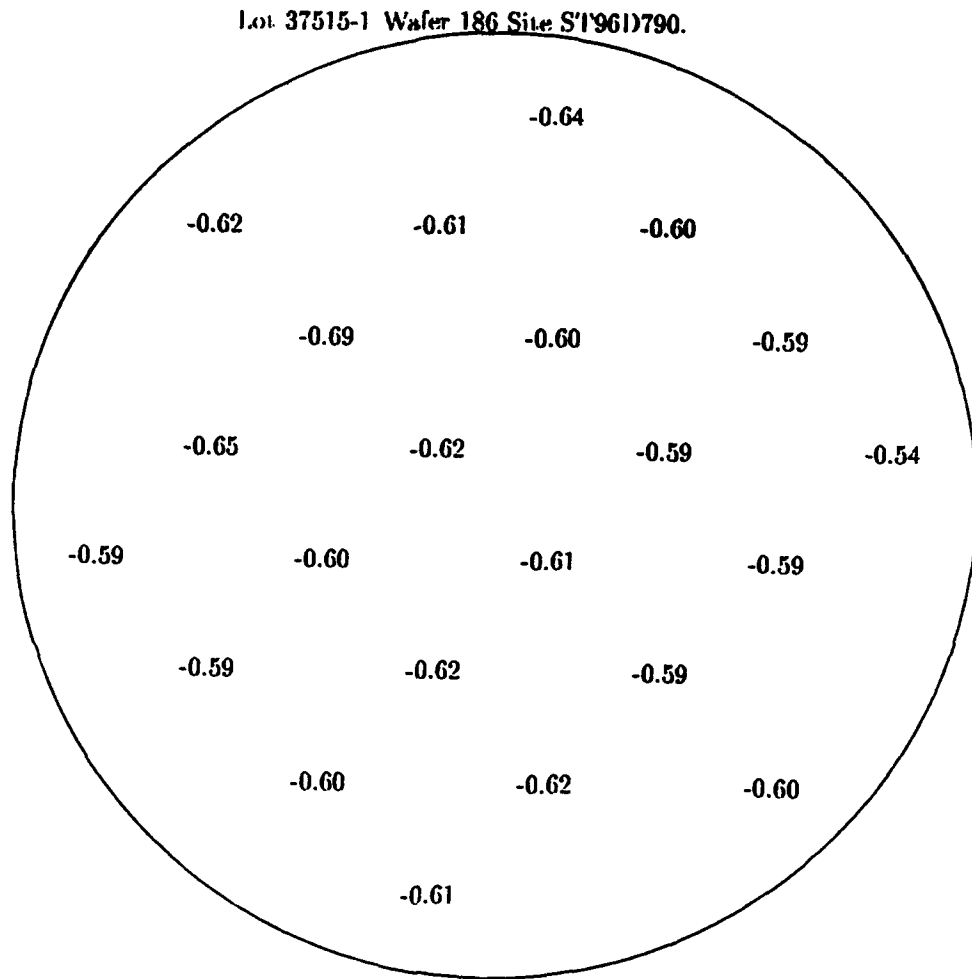


Figure 4.2: Se profiles calculated for the Lot 1 process from Suprem3.5.



1

Figure 4.3: Threshold voltage mapping of a Lot 1 Si implanted wafer.



1

Figure 4.4: Threshold voltage mapping for a Lot 1 Se implanted wafer.

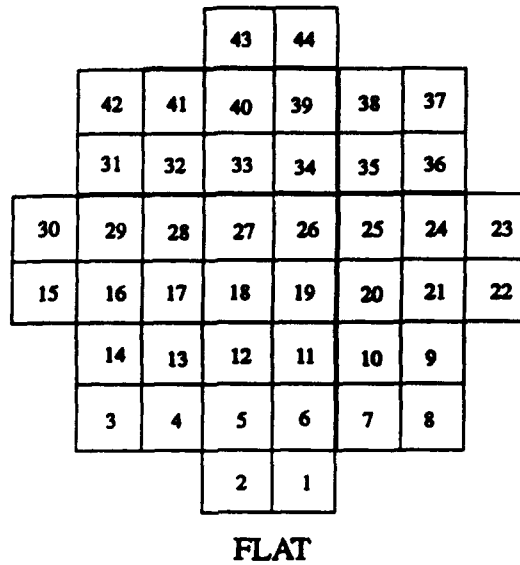


Figure 4.5: Layout for each 3 inch wafer.

4.3 Wafer Testing

Each 3 inch wafer is divided into 44 usable grids and identical devices are fabricated in each grid. The wafer layout is shown in Figure 4.5.

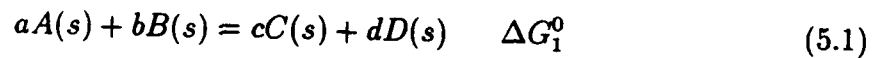
The devices selected for testing including gate lengths of 0.5, 0.7, 1.1, 2.0, 5.0 μm and device oriented at 0, ± 45 , 90 degree to the major axis for both implant species. This totals to 40 distinct devices tested in each grid. Half of the 44 grids are stepped over via an automatic testing probe. As a result, a total of 880 MESFETs are tested on each wafer and the resulting threshold voltages are compiled in formatted ascii files. For each lot, threshold voltage data is obtained for 12320 discrete devices.

Chapter 5

Equilibrium Properties of Pure GaAs

5.1 The Thermodynamics of Chemical Reactions

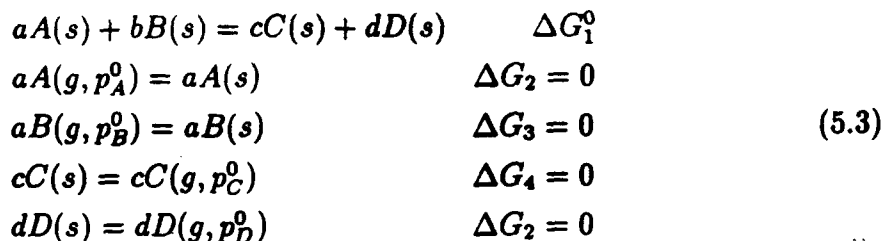
Under constant pressure, equilibrium is characterized by a minimum in the Gibbs free energy. Let us consider the following chemical reaction:



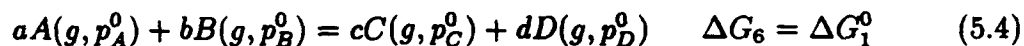
The change in Gibbs free energy is of course given by:

$$\Delta G = \Delta H - T\Delta S \quad (5.2)$$

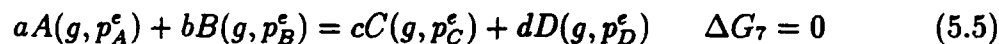
Let p_A^0 , p_B^0 , p_C^0 and p_D^0 be the equilibrium partial pressures of the pure components. Then we may convert the above reaction (5.1) into one involving the gaseous components of the constituents only, [26].



Adding up the above equations, we obtain:



The free energy change ΔG_2 to ΔG_5 are all zero because the p_i^0 are chosen to be the equilibrium values for the pure components. Let us now choose another set of partial pressures p_A^e , p_B^e , p_C^e , p_D^e so that the reaction 5.4 will be in equilibrium. Hence the change in Gibbs free energy will be zero.



Next, we need to calculate the change of Gibbs free energy for each pure substance from a partial pressure of p_i^0 to p_i^e so that we can find a relationship between ΔG_1^0 to ΔG_7 . The thermodynamic function satisfied by the Gibbs free energy is:

$$dG = Vdp - SdT \tag{5.6}$$

Let the change of partial pressure take place under constant temperature and further assume the vapors to be an ideal gas, then $pV = RT$ and we obtain:

$$dG = Vdp = \frac{RT}{p} dp \tag{5.7}$$

$$\Delta G = RT \ln \frac{p_i^e}{p_i^0} \quad (5.8)$$

Substituting A, B, C and D into the above equation, we obtain;

$$\begin{aligned} aA(g, p_A^0) + bB(g, p_B^0) &= cC(g, p_C^0) + dD(g, p_D^0) & \Delta G_6 &= \Delta G_1^0 \\ aA(g, p_A^e) &= aA(g, p_A^0) & \Delta G_8 &= aRT \ln \frac{p_A^0}{p_A^e} \\ bB(g, p_B^e) &= bB(g, p_B^0) & \Delta G_9 &= bRT \ln \frac{p_B^0}{p_B^e} \\ cC(g, p_C^0) &= cC(g, p_C^e) & \Delta G_{10} &= cRT \ln \frac{p_C^e}{p_C^0} \\ dD(g, p_D^0) &= dD(g, p_D^e) & \Delta G_{11} &= dRT \ln \frac{p_D^e}{p_D^0} \\ aA(g, p_A^e) + bB(g, p_B^e) &= cC(g, p_C^e) + dD(g, p_D^e) & \Delta G_7 &= 0 \end{aligned} \quad (5.9)$$

Upon summation of all the free energy changes,

$$\Delta G_7 = 0 = \Delta G_6 + \Delta G_8 + \Delta G_9 + \Delta G_{10} + \Delta G_{11} \quad (5.10)$$

$$0 = \Delta G_1^0 + RT \ln \frac{(p_C^e/p_C^0)^c (p_D^e/p_D^0)^d}{(p_A^e/p_A^0)^a (p_B^e/p_B^0)^b} \quad (5.11)$$

We see that the argument of the logarithmic function depends only on the temperature of the reaction and is independent of a, b, c, and d. We call this the equilibrium constant K.

$$\Delta G^0 = -RT \ln K \quad (5.12)$$

Let's define the *activity* of a component as:

$$a_i \equiv \frac{p_i}{p_i^0} \quad (5.13)$$

Then, the equilibrium constant can be written as:

$$K = \frac{(a_C^e)^c (a_D^e)^d}{(a_A^e)^a (a_B^e)^b} = \frac{\prod (a_i^e)^{n_i} (\text{Products})}{\prod (a_i^e)^{n_i} (\text{Reactants})} \quad (5.14)$$

5.2 Dilute Solution and Henry's Law

Consider a solution of n solute atoms and $N-n$ solvent atoms. Define the atom fraction as:

$$X = \frac{n}{N} \quad (5.15)$$

Let the partial vapor pressure of solute atoms be p_i and the vapor pressure of the pure substance be p_i^0 . Then if $X = 1$, obviously we would have $p_i = p_i^0$. On the other hand, if $X = 0$, then $p_i = 0$. An ideal solution is defined as one in which the vapor pressure of a component i is a linear function of composition:

$$p_i = X_i p_i^0 \quad (5.16)$$

This is known as Raoult's Law. Comparing this with equation 5.13:

$$\Rightarrow a_i = X_i \quad (5.17)$$

Most real solutions do not fall into this category. However, as long as the separation between solute atoms are large and the interaction is small, we may use the dilute solution approximation.

$$p_i = b X_i \quad (5.18)$$

The above equation suggests that the thermodynamic properties of the solute are additive for dilute solutions. Thus, the vapor pressure of a solution containing two hundred atoms would be twice that containing one hundred atoms. Here b is a constant whose value depends on the nature of the solute and solvent. This is known as Henry's Law.

Again, from the definition of activity, we obtain:

$$a_i = \frac{b}{p_i^0} X_i \quad \text{or} \quad a_i = \gamma_i X_i \quad (5.19)$$

where γ is called the activity coefficient, $\gamma_i = 1$ for an ideal solution. It is constant for a given solute in a dilute solution independent of concentration.

Table 5.1: Defect Nomenclature

Ga_{Ga}	Ga atom on Ga site
As_{As}	As atom on As site
Ga_i	Ga atom on interstitial site
As_i	As atom on interstitial site
Ga_{As}	Ga atom on As site, anti-site defect
As_{Ga}	As atom on Ga site, anti-site defect
F_{Ga}	Foreign atom on Ga site
F_{As}	Foreign atom on As site
F_i	Foreign atom on interstitial site
V_{Ga}	Vacancy of Ga site
V_{As}	Vacancy of As site
e^-	Electron in conduction band
h^+	Hole in valence band

For an dilute solution, the equilibrium constant in equation 5.14 is given by:

$$K = \frac{(X_C)^c (X_D)^d}{(X_A)^a (X_B)^b} = \frac{[C]^c [D]^d}{[A]^a [B]^b} \quad (5.20)$$

where the square brackets indicates the atomic concentration of an element and the activity coefficient has been absorbed into the equilibrium constants.

5.3 Defect Nomenclature

Three basic types of defects may occur in a crystal. An unoccupied lattice site is called a vacancy. An atom occupying a non-lattice site is called an interstitial. In addition, foreign atoms can occupy either the vacancy or interstitial sites. Table 5.3 lists the defect nomenclature.

When writing reaction equations involving defects, three considerations must apply as follows [26]:

1. Total charge must be conserved on both sides of the equation.
2. Mass must be conserved on both sides of the equation.

3. Fixed proportion of Ga and As sites must be created regardless of whether or not they are actually occupied or not.

For a compound semiconductor such as GaAs, the site ratio between Ga and As as well as the gross composition must be preserved; therefore, different types of defects can not occur arbitrarily. There are six basic types of combinations as follows [27]:

1. Schottky disorder involving vacancies, V_{Ga} and V_{As} .
2. interstitial disorder involving interstitial atoms, Ga_i and As_i .
3. anti-structure disorder involving misplaced atoms, Ga_{As} and As_{Ga} .
4. Schottky interstitial disorder involving vacancies and interstitials for the same type of atom, e.g., $V_{Ga} + Ga_i$ or $V_{As} + As_i$. This type of defect combination is usually called a Frenkel defect.
5. Schottky anti-Site disorder involving vacancies and misplaced atoms for the same type of atom, e.g., $V_{Ga} + Ga_{As}$ or $V_{As} + As_{Ga}$.
6. Interstitial anti-site disorder involving interstitial atoms of one type and misplaced atoms of the other type, e.g., $Ga_i + As_{Ga}$ or $As_i + Ga_{As}$.

5.4 Native Defects of GaAs

5.4.1 Schottky Defects

For semi-insulating GaAs, there are usually more As than Ga atoms. If Schottky defects are the only disorder, then there must be an equivalent number of Ga vacancies to accommodate for this.

$$N_V = N_{As} - N_{Ga} \quad (5.21)$$

In thermal equilibrium, vacancies of both type will be formed due to the entropy change brought about by the vacancies.

$$V_{Ga} + V_{As} \rightleftharpoons 0 \quad (5.22)$$

Assume M_V vacancies of Ga and As are formed through this process, the general form of the Gibbs free energy is given by [27]:

$$G = N_{Ga}\mu(Ga) + N_{As}\mu(As) + (N_V + M_V)\mu(Ga) + M_V\mu(As) - TS_{config} \quad (5.23)$$

Where μ is the chemical potential of the species. $S_{config} = k \ln W$ where W is the statistical distribution of vacancies on the available sites and is the product of two the factors:

1. N_{Ga} atoms and $(N_V + M_V)$ vacancies distributed over $(N_{Ga} + N_V + M_V)$ sites.
2. N_{As} atoms and M_V vacancies distributed over $(N_{As} + M_V)$ sites.

Then:

$$W = W_1 W_2 = \frac{(N_{As} + M_V)!(N_{Ga} + N_V + M_V)!}{N_{Ga}!(N_V + M_V)!N_{As}!M_V!} \quad (5.24)$$

Using Stirling's approximation, $\ln N! = N \ln N - N$, we find:

$$S_{config} = -k(N_{Ga} \ln[Ga_{Ga}] + (N_V + M_V) \ln[V_{Ga}]) - (N_{As} \ln[As_{As}] + M_V \ln[V_{As}]) \quad (5.25)$$

where the square brackets indicate the site fractions.

$$[V_{Ga}] = \frac{N_V + M_V}{N_{Ga} + N_V + M_V} \quad (5.26)$$

$$[V_{As}] = \frac{M_V}{N_{As} + M_V} \quad (5.27)$$

The number of vacancies formed in thermal equilibrium is determined by minimizing the Gibbs free energy:

$$\left(\frac{\partial G}{\partial M_V} \right)_{N_{Ga}, N_{As}, P, T} = \mu(V_{Ga}) + kT \ln[V_{Ga}] + \mu(V_{As}) + kT \ln[V_{As}] = 0 \quad (5.28)$$

Resulting in

$$[V_{Ga}][V_{As}] = K_S \quad (5.29)$$

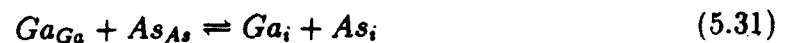
where

$$K_S = \exp(-(\mu(V_{Ga}) + \mu(V_{As}))/kT) \quad (5.30)$$

The exact same relationship can also be obtained by mass action considerations.

5.4.2 Interstitial Defect

The interstitial defect can be described by the following reaction:



According to the mass action law:

$$\frac{[Ga_i][As_i]}{[Ga_{Ga}][As_{As}]} = K_i \quad (5.32)$$

Since the amount of defect atoms are much smaller than the amount of Ga or As atoms. The site fractions of Ga and As are:

$$[Ga_{Ga}] \approx 1 \quad \text{and} \quad [As_{As}] \approx 1 \quad (5.33)$$

Resulting in the approximation:

$$[Ga_i][As_i] = K_i \quad (5.34)$$

5.4.3 Anti-site Defect

The anti-site defect plays an important role in the electrical properties of GaAs. The deep donor EL2 is associated with the As anti-site, As_{Ga} , and is responsible for compensating the residual carbon acceptors to give LEC GaAs its semi-insulating property.

The equilibrium of anti-sites is described as:



$$\frac{[Ga_{As}][As_{Ga}]}{[Ga_{Ga}][As_{As}]} = K_A \quad (5.36)$$

Again, for small amount of defects, $[Ga_{Ga}] = [As_{As}] \approx 1$, and the above equation simplifies to:

$$[Ga_{As}][As_{Ga}] = K_A \quad (5.37)$$

Once again, a simple product relationship exists for anti-site structures as with Schottky and interstitial disorder.

5.4.4 Frenkel Defect

This type of defect was first observed by Frenkel and arises from the transfer of atoms from lattice to interstitial sites. It's the most important of the asymmetrical type of defect.



From the mass action law:

$$\frac{[Ga_i][V_{Ga}]}{[Ga_{Ga}]} = K_1 \quad (5.40)$$

$$\frac{[As_i][V_{As}]}{[As_{As}]} = K_2 \quad (5.41)$$

Approximating the site fraction of Ga and As to be 1, results in:

$$\Rightarrow [Ga_i][V_{Ga}] = K_1 \quad \text{and} \quad [As_i][V_{As}] = K_2 \quad (5.42)$$

Multiplying the above two equations together and using equation 5.28, we obtain:

$$[Ga_i][As_i] = \frac{K_1 K_2}{K_S} \quad (5.43)$$

5.4.5 Schottky Anti-site Defect

The hybrid defect of the Schottky and anti-structure disorder is described by:



$$\frac{[Ga_{As}][V_{Ga}]^2}{[Ga_{Ga}]} = K_{sa1} \quad (5.46)$$

$$\frac{[As_{Ga}][V_{As}]^2}{[As_{As}]} = K_{sa2} \quad (5.47)$$

5.4.6 Interstitial Anti-site Defect

The hybrid defect of the interstitial and anti-site defect is described by:



$$\frac{[Ga_{As}][As_i]^2}{[Ga_{Ga}][As_{As}]^2} = K_{IA} \quad (5.49)$$

$$[Ga_{As}][As_i]^2 = K_{IA} \quad (5.50)$$

Similar relations hold for the case involving As_{Ga} and Ga_i .

5.5 Equilibrium Properties of GaAs

5.5.1 Pure GaAs

Due to the compound nature of GaAs, the intrinsic defect structure is much more complex than an elemental semiconductor such as Si. In GaAs, there are two types of vacancies, two kinds of interstitials and two kinds of anti-site structures to be accounted for. The following reaction describes the equilibrium properties of crystalline GaAs.



$$0 = V_{Ga} + V_{As} \quad (5.52)$$

$$V_{Ga}^0 = V_{Ga}^- + h^+ \quad (5.53)$$

$$V_{As}^0 = V_{As}^+ + e^- \quad (5.54)$$

$$Ga_{Ga} + V_{As} = Ga_{As} + V_{Ga} \quad (5.55)$$

$$As_{As} + V_{Ga} = As_{Ga} + V_{As} \quad (5.56)$$

$$Ga_{Ga} = Ga_i + V_{Ga} \quad (5.57)$$

$$As_{As} = As_i + V_{As} \quad (5.58)$$

$$\frac{1}{4}As_4(g) + V_{As}^0 = As_{As}^0 \quad (5.59)$$

The mass action relationships for the above equations are:

$$[e^-][h^+] = K_i \quad (5.60)$$

$$[V_{Ga}][V_{As}] = K_S \quad (5.61)$$

$$\frac{[h^+][V_{Ga}^-]}{V_{Ga}^0} = K_a \quad (5.62)$$

$$\frac{[e^-][V_{As}^+]}{V_{As}^0} = K_d \quad (5.63)$$

$$\frac{[Ga_{As}][V_{Ga}]}{[V_{As}]} = K_{a1} \quad (5.64)$$

$$\frac{[As_{Ga}][V_{As}]}{[V_{Ga}]} = K_{a2} \quad (5.65)$$

$$[Ga_i][V_{Ga}] = K_{i1} \quad (5.66)$$

$$[As_i][V_{As}] = K_{i2} \quad (5.67)$$

$$[V_{As}] = (K_{As} p_{As_4}^{\frac{1}{4}})^{-1} \quad (5.68)$$

One must also consider the charge neutrality condition:

$$[e^-] + [V_{Ga}^-] = [h^+] + [V_{As}^+] \quad (5.69)$$

The results of this is that we have 10 equations and 11 unknowns. We will express all the quantities in terms of the As pressure, p_{As} . There are three regions of interest to us. If the material is p-type then the concentration of electrons and the ionized donors is neglected. For semi-insulating material case $[e^-] = [h^+]$, and for the n-type material case, $[V_{As}^+] = [e^-]$. These regions are summarized as follows:

$$\begin{aligned} \text{Region One : } & [V_{Ga}^-] = [h^+] \quad \text{p type material} \\ \text{Region Two : } & [e^-] = [h^+] \quad \text{Intrinsic material} \\ \text{Region Three : } & [V_{As}^+] = [e^-] \quad \text{n type material} \end{aligned} \quad (5.70)$$

Assume $x = K_{As} p_{As}^{\frac{1}{4}}$. The neutral defects can be solved independent of the regions and are given as:

$$[V_{As}] = x^{-1} \quad (5.71)$$

$$[V_{Ga}] = K_S x \quad (5.72)$$

$$[Ga_{As}] = \frac{K_{a1}}{K_S} x^{-2} \quad (5.73)$$

$$[As_{Ga}] = K_{a2} K_S x^2 \quad (5.74)$$

$$[Ga_i] = \frac{K_{i1}}{K_S} x^{-1} \quad (5.75)$$

$$[As_i] = K_{i2} x \quad (5.76)$$

In region 1, the following equations hold:

$$[h^+] = [V_{Ga}^-] = \sqrt{K_a K_S} x^{1/2} \quad (5.77)$$

$$[e^-] = \frac{K_i}{\sqrt{K_a K_S}} x^{-1/2} \quad (5.78)$$

$$[V_{As}^+] = \frac{K_d \sqrt{K_a K_S}}{K_i} x^{-1/2} \quad (5.79)$$

In region 2, we have:

$$[e^-] = [h^+] = \sqrt{K_i} \quad (5.80)$$

$$[V_{Ga}^-] = \frac{K_a K_S}{\sqrt{K_i}} x \quad (5.81)$$

$$[V_{As}^+] = \frac{K_d}{\sqrt{K_i}} x^{-1} \quad (5.82)$$

In region 3, the solutions are:

$$[V_{As}^+] = [e^-] = \sqrt{K_d} x^{-1/2} \quad (5.83)$$

$$[h^+] = \frac{K_i}{\sqrt{K_d}} x^{1/2} \quad (5.84)$$

$$[V_{Ga}^-] = \frac{K_a K_S \sqrt{K_d}}{K_i} x^{1/2} \quad (5.85)$$

If the natural logarithm of various concentrations is plotted against the logarithm of x , the graph consists of straight lines. We show this in Figure 5.1 and the diagram is known as a Kroger-Vink diagram [28]. The exact position of the lines can not be determined unless we know the value of all the equilibrium constants in detail.

Implanted GaAs is subjected to high temperature anneals in which the equilibrium of the various defects are established. As the crystal cools down, the atomic defects usually don't have enough thermal energy to diffuse to new sites in order to establish new equilibrium at room temperature. As a result, the defects are "frozen in." The electronic defects, however are much more mobile and will establish an equilibrium with the "frozen in" atomic defects. Therefore, in figure 5.1, the electron and hole concentrations decrease while the various charged defects tend to become neutral.

5.5.2 GaAs with Carbon and EL2

LEC grown semi-insulating GaAs contains residual carbon that is compensated by the deep native donor EL2, that is associated with the As anti-site. To describe the

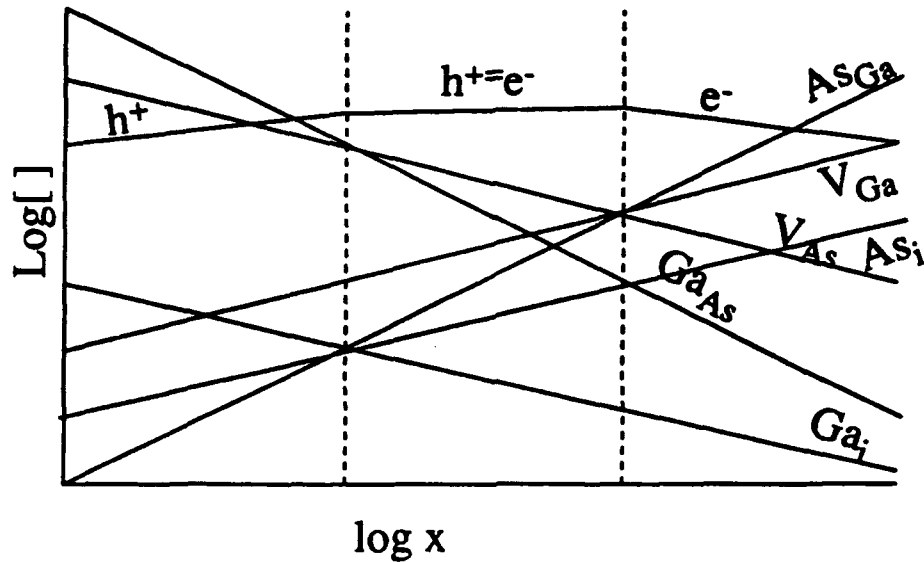


Figure 5.1: Kroger-Vink Diagram of Pure GaAs

equilibrium configuration of LEC GaAs, we add three more equations to the general equilibrium equations discussed for pure GaAs from the last section. We also need a new neutrality condition.

$$\frac{1}{4}C_A(g) + V_{As} = C_{As} \quad (5.86)$$

$$C_{As} = C_{As}^+ + e^- \quad (5.87)$$

$$As_{Ga} = As_{Ga}^- + h^+ \quad (5.88)$$

The neutrality condition is now:

$$[e^-] + [As_{Ga}^-] = [h^+] + [C_{As}^+] \quad (5.89)$$

At elevated temperatures (1000K), the neutrality condition can simply be approximated by $[e^-] = [h^+]$ since carbon and EL2 levels are typically around $1 \times 10^{16} \text{ cm}^{-3}$. However, at room temperature, the neutrality condition is approximated as $[As_{Ga}^-] = [C_{As}^+]$. In either case, solutions are obtained as described in the last section.

Chapter 6

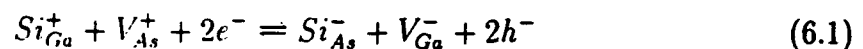
Activation Model: Si and Se

Silicon and selenium are the most widely used n-type dopants in GaAs. Si activation has been widely studied in the last ten or so years with Se activation recently receiving more attention. Experimentally, reported values for Si and Se activation varies widely from as low as 40% to near 100% [29, 30, 31].

6.1 Si activation

Silicon is an amphoteric dopant in GaAs. It acts as a donor when occupying the Ga site and as an acceptor when occupying the As site. Therefore, the active donor concentration is given by the difference between the Si occupying the Ga and As sites. In our investigation, we only consider the charged defects EL2 and carbon. The deep level EL2 is present in GaAs in the range of around $1 \times 10^{16} \text{ cm}^{-3}$, while carbon is typically found to be around $2 \times 10^{15} \text{ cm}^{-3}$.

Several theoretical explanations described the activation of Si in GaAs. An early theory developed by Greiner is based on the following equation [32].



By utilizing the law of mass action and $p = n_i^2/n$, the ratio of Si occupying the As

and Ga sites may be obtained as:

$$\frac{[Si_{As}^-]}{[Si_{Ga}^+]} = \frac{1}{K} \frac{[V_{As}^+]}{[V_{Ga}^-]} \left(\frac{n}{n_i}\right)^4 \quad (6.2)$$

Greiner defines the saturation electron concentration, n_{sat} as the electron concentration occurring when $[Si_{As}^-]/[Si_{Ga}^+] = 1$. Then:

$$\frac{n_{sat}}{n_i} = \left\{ K \frac{[V_{Ga}^-]}{[V_{As}^+]} \right\}^{\frac{1}{4}} = K_V \quad (6.3)$$

where K_V is fitted as a constant dependent only on temperature.

Although the charged vacancies can be neglected in the neutrality condition since their concentrations are typically much lower than the intrinsic carrier density at an elevated annealing temperature. This does not imply that the charged vacancy concentrations are not influenced by the electron concentration. The relationships between the ionized and neutral vacancies are:

$$[V_{As}^+] = \frac{[V_{As}^0]}{1 + g \exp\left(\frac{E_F - E_{V_{As}^+}}{kT}\right)} \quad (6.4)$$

$$[V_{Ga}^-] = \frac{[V_{Ga}^0]}{1 + g \exp\left(\frac{E_{V_{Ga}^-} - E_F}{kT}\right)} \quad (6.5)$$

As the electron concentration changes due to different amount of doping, the Fermi level shifts as well. As a result, the amount of ionized vacancies change as well. The concentrations of V_{Ga}^- and V_{As}^+ change in opposite directions while their product remains constant, as required by mass action law.

In the theory proposed by Bindal et al [33], neutral vacancies are used as the starting point and the equilibrium conditions for Si on Ga and As sites are proposed as:

$$Si_{Ga} + V_{As} = Si_{As} + V_{Ga} \quad (6.6)$$

$$\Rightarrow \frac{[Si_{As}]}{[Si_{Ga}]} = \frac{1}{K} \frac{[V_{As}]}{[V_{Ga}]} \quad (6.7)$$

Solving this together with the total Si concentration, given as:

$$[Si]_{total} = [Si_{Ga}] + [Si_{As}] \quad (6.8)$$

Since for an n-type semiconductor, most of the shallow donors as well as acceptors are ionized, the total Si concentration is actually given by:

$$[Si]_{total} = [Si_{Ga}] + [Si_{As}] + [Si_{Ga}^+] + [Si_{As}^-] \quad (6.9)$$

and can be approximated as:

$$[Si]_{total} = [Si_{Ga}^+] + [Si_{As}^-] \quad (6.10)$$

As a result, the mass action equation proposed by Bindal et al. is not complete and must also include terms for the ionization of Si_{Ga} and Si_{As} .

Vanasupa proposed a theory based on the following mass action equation [34].

$$Si_{Ga}^+ + V_{As}^0 + e^- = Si_{As}^- + V_{Ga}^0 + h^+ \quad (6.11)$$

As a result, the ratio of Si on As sites to those on Ga sites is written as:

$$\frac{[Si_{As}^-]}{[Si_{Ga}^+]} = K \frac{[V_{As}^0] n^2}{[V_{Ga}^0] n_i^2} = \Omega \left(\frac{n}{n_i}\right)^2 \quad (6.12)$$

where Ω is fitted as a constant dependent only on temperature.

Although the product of the neutral vacancies must remain constant when equilibrium is reached at a particular temperature, the ratio of the two does not. This ratio is intimately connected with the stoichiometry of the material as well as the distribution of dislocations.

To systematically study the activation of dopants in GaAs, let's first list all the relevant mass action equations. The reactions concerning pure GaAs include:

$$0 = e^- + h^+ \quad (6.13)$$

$$0 = V_{Ga} + V_{As} \quad (6.14)$$

$$\frac{1}{4}As_4(g) + V_{As} = As_{As} \quad (6.15)$$

The EL2 defect is represented by As_{Ga} and the relevant reactions include:

$$As_{As} + V_{Ga} = As_{Ga} + V_{As} \quad (6.16)$$

$$As_{Ga} = As_{Ga}^+ + e^- \quad (6.17)$$

Equations describing carbon incorporation into the GaAs lattice are:

$$C(g) + V_{As} = C_{As} \quad (6.18)$$

$$C_{As} = C_{As}^- + h^+ \quad (6.19)$$

and the relations involving Si incorporation into the GaAs lattice are:

$$Si(g) + V_{Ga} = Si_{Ga} \quad (6.20)$$

$$Si(g) + V_{As} = Si_{As} \quad (6.21)$$

$$Si_{Ga} = Si_{Ga}^+ + e^- \quad (6.22)$$

$$Si_{As} = Si_{As}^- + h^+ \quad (6.23)$$

The neutrality condition now reads:

$$[e^-] + [C_{As}^-] + [Si_{As}^-] = [h^+] + [As_{Ga}^+] + [Si_{Ga}^+] \quad (6.24)$$

There are now a total of 12 equations and 15 unknowns. As a result, each quantity may be expressed as a function of 3 other variables. Note that adding each new element such as carbon or Si adds one more variable than equation.

From the reactions describing the incorporation of Si into GaAs lattice, we obtain:

$$[Si_{Ga}] = K_1[V_{Ga}]p_{Si} \quad (6.25)$$

$$[Si_{As}] = K_2[V_{As}]p_{Si} \quad (6.26)$$

$$\frac{[Si_{Ga}^+][e^-]}{[Si_{Ga}^0]} = K_D = \frac{[Si_{Ga}^+][e^-]}{K_1[V_{Ga}]p_{Si}} \quad (6.27)$$

$$\Rightarrow [Si_{Ga}^+] = \frac{K_D K_1 [V_{Ga}] p_{Si}}{[e^-]} \quad (6.28)$$

Similarly, we can derive an equation for $[Si_{As}]$.

$$[Si_{As}^-] = \frac{K_A K_2 [V_{As}] p_{Si}}{[h^+]} \quad (6.29)$$

Taking the ratio of the above two equations, results in:

$$\frac{[Si_{As}^-]}{[Si_{Ga}^+]} = \frac{K_A K_2 [V_{As}] n^2}{K_D K_1 [V_{Ga}] n_i^2} = \alpha \frac{[V_{As}] n^2}{[V_{Ga}] n_i^2} \quad (6.30)$$

where we have written $[e^-] = n$, $[h^+] = p$ and $np = n_i^2$.

The relationships for the anti-structures are:

$$\frac{[V_{As}][As_{Ga}]}{[V_{Ga}]} = K_{a1} \quad (6.31)$$

$$\Rightarrow \frac{[V_{As}]}{[V_{Ga}]} = \frac{K_{a1}}{[As_{Ga}]} = \frac{K_{a1}}{N_{EL2}} \quad (6.32)$$

$$\Rightarrow \frac{[Si_{As}^-]}{[Si_{Ga}^+]} = \frac{\alpha n^2}{N_{EL2} n_i^2} \quad (6.33)$$

where the extra equilibrium constant is absorbed into α . The use of the neutral EL2 concentration is appropriate in this equation since in n-type material the EL2 remains neutral because the Fermi level is much higher than the EL2 energy level. The concentration of neutral EL2 remains relatively constant and is essentially independent of the electron density.

We know that carbon and EL2 are present in significant amounts in GaAs. The relationships between ionized impurities and total impurities are given by:

$$N_D^+ = \frac{N_D}{1 + g \exp\left(\frac{E_F - E_D}{KT}\right)} \quad (6.34)$$

$$N_A^+ = \frac{N_A}{1 + g \exp\left(\frac{E_A - E_F}{kT}\right)} \quad (6.35)$$

For n-typed semiconductors at a temperature of around 1000K, the temperature where implanted dopants are usually annealed, virtually all the carbon is ionized. On the other hand, EL2, being a mid-gap deep donor, less than 1% of it is ionized. As a result, we neglect the concentration of charged EL2 and use the total concentration of carbon in the neutrality equation. This condition breaks down however, when the donor level in GaAs falls below that of the acceptor level. In this case, the neutrality condition must include the ionized EL2 concentration and the neutral EL2 concentration becomes highly influenced by the carrier density. Our ratio equation for Si on the As and Ga sites must also be revised to include this effect. However, for the case of the donor level being less than that of the acceptor is not of interest to us since this occurs well into the substrate not in the active channel region.

If we further assume that virtually all of the Si dopant atoms are ionized, then we arrive at the three equations which governs the activation of the Si atoms.

$$\frac{[Si_{As}^-]}{[Si_{Ga}^+]} = \frac{\alpha}{N_{EL2}} \frac{n^2}{n_i^2} \quad (6.36)$$

$$n + N_C + [Si_{As}^-] = \frac{n_i^2}{n} + [Si_{Ga}^+] \quad (6.37)$$

$$[Si_{As}^-] + [Si_{Ga}^+] = [Si]_{total} \quad (6.38)$$

Letting $x = [Si_{As}^-]$, $y = [Si_{Ga}^+]$, $t = [Si]_{total}$ and $\Omega = \alpha/N_{EL2}$, resulting in:

$$\Rightarrow x - y = \frac{n_i^2}{n} - n - N_C \text{ and } x + y = t \quad (6.39)$$

$$x = \frac{1}{2} \left(t + \frac{n_i^2}{n} - n - N_C \right) \quad (6.40)$$

$$y = \frac{1}{2} \left(t - \frac{n_i^2}{n} + n + N_C \right) \quad (6.41)$$

$$\frac{x}{y} = \frac{t + \frac{n_i^2}{n} - n - N_C}{t - \frac{n_i^2}{n} + n + N_C} = \Omega n^2 \quad (6.42)$$

Multiplying out the above equations, we obtain:

$$\Omega n^4 + \Omega(N_C + t)n^3 + (1 - \Omega)n_i^2 n^2 + (N_C - t)n_i^2 n - n_i^4 = 0 \quad (6.43)$$

For each fitting constant Ω , the above equation is solved to obtain n . By substituting n into equation 6.36, we obtain the activation efficiency as:

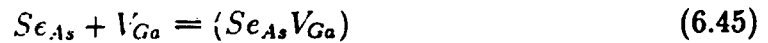
$$\eta = \frac{[Si_{Ga}^+] - [Si_{As}^-]}{[Si_{Ga}^+] + [Si_{As}^-]} = \frac{n_i^2 - \Omega n^2}{n_i^2 + \Omega n^2} \quad (6.44)$$

where n_i is calculated at the annealing temperature.

6.2 Se Activation

The first comprehensive theory for Se activation in GaAs was proposed by Lidow et al [35]. They recognized the importance of the complex formed by a Se atom and a gallium vacancy. It is in fact the mechanism by which Se diffuses. It also plays an important role in determining the amount of Se occupying As sites and thereby being a donor.

The reaction process for Se activation is described by the following equations:



$$K_1 = \frac{[Se_{As}V_{Ga}]}{[Se_{As}][V_{Ga}]} \quad (6.47)$$

$$K_2 = \frac{[Se_{As}^+]n}{[Se_{As}]} \quad (6.48)$$

$$\Rightarrow \frac{[Se_{As}^+]}{[Se_{As}V_{Ga}]} = \frac{K_2}{K_S K_1} \frac{[V_{As}]}{n} \quad (6.49)$$

where we have used the relationship between neutral vacancies. In addition, we also

have the occurrence of the Schottky anti-site defect:

$$As_{As} = As_{Ga} + 2V_{As} \quad (6.50)$$

$$\Rightarrow [V_{As}] = \sqrt{\frac{K_{SA}}{N_{EL2}}} \quad (6.51)$$

We finally arrive at the desired equation:

$$\frac{[Se_{As}^+]}{[Se_{As}V_{Ga}]} = \frac{K_2\sqrt{K_{SA}}}{K_S K_1} \frac{1}{\sqrt{N_{EL2}n}} = \frac{\Omega'n_i}{n} \quad (6.52)$$

where we have inserted an n_i in order to keep the fitting constant unitless. The neutrality condition in this case reads:

$$[e^-] + [C_{As}^-] = [h^+] + [Se_{As}^+] \quad (6.53)$$

In addition, the total concentration of Se is given by:

$$[Se_{As}^+] + [Se_{As}V_{Ga}] = [Se]_{total} \quad (6.54)$$

$$\Rightarrow [Se_{As}^+] = n + N_C - \frac{n_i^2}{n} \quad (6.55)$$

$$[Se_{As}V_{Ga}] = t - n - N_C + \frac{n_i^2}{n} \quad (6.56)$$

where t is the total amount of Se implanted. As a result:

$$\frac{n + N_C - \frac{n_i^2}{n}}{t - n - N_C + \frac{n_i^2}{n}} = \frac{\Omega'n_i}{n} \quad (6.57)$$

Multiplying out the above equation, results in:

$$n^3 + (N_C + \Omega'n_i)n^2 - (n_i^2 + \Omega'n_it - \Omega'n_iN_C)n - \Omega'n_i^3 = 0 \quad (6.58)$$

Once again, the above equation is solved to obtain n . Substituting this value of n

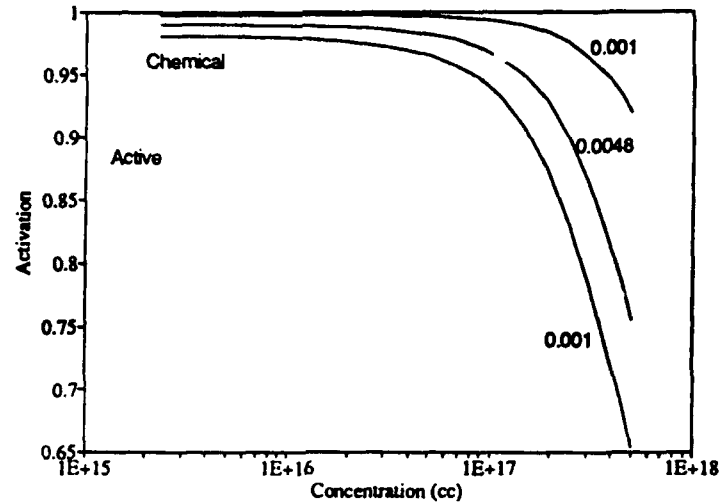


Figure 6.1: Si Activation as a Function of Concentration.

into equation 6.51, we obtain the activation efficiency for Se in GaAs:

$$\eta = \frac{[Se_{As}^+]}{[Se_{As}^+] + [Se_{As}V_{Ga}]} = \frac{\Omega'n_i}{\Omega'n_i + n} \quad (6.59)$$

6.3 Discussion

The activation of Si and Se in GaAs was comprehensively studied by J. K. Dhiman and K. L. Wang [36]. Their result is implemented in the SUPREM3.5 process modeling program for GaAs[37]. By fitting Ω and Ω' as a constant, we may obtain the activation efficiency as a function of the total dopant concentration. Figure 6.1 and 6.2 plots activation curves calculated using different fitting constants. The activation of both Si and Se is seen to decrease as the dopant concentration increases. Larger Si activations are obtained for smaller fitting constants; while larger Se activation is obtained for larger fitting constants. The shape of our curves are consistent with Dhiman's data.

We used Suprem3.5 to calculate the dopant profiles for the Lot 1 implant process. We also fitt our activation model to calculations produced by Suprem3.5, whose

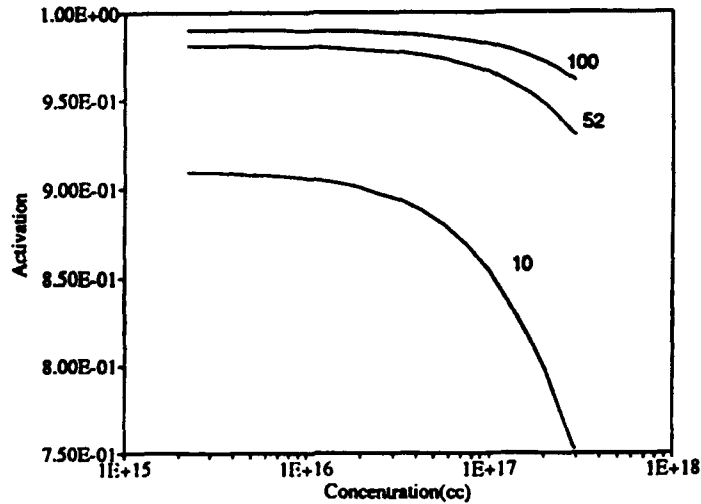


Figure 6.2: Se Activation as a Function of Concentration.

activation model is experimentally based. Figure 6.3 and 6.4 show the result of these calculations. The constants Ω and Ω' are selected so that at the highest dopant concentrations, the activation efficiency of our model matches those calculated by Suprem3.5. Figure 6.3 shows that the activation of Si predicted by our model is lower than those that predicted by Suprem3.5. Figure 6.4 shows the activation predicted for Se by our model is higher than those predicted by Suprem3.5. This result is internally consistent with our model and shows that the site occupation of Si_{Ga} is proportional to EL2 while the Se occupation of the As site is inversely proportional to the square root of EL2. This result is also consistent with the reported depth distribution of EL2 in ion implanted LEC GaAs [38, 39].

For these situations, the EL2 concentration is typically higher at the surface, gradually falling to a constant value well into the substrate. Since we fit our Ω and Ω' at the highest concentration of our dopant profile which is always near the surface. Deeper in the substrate, where the EL2 level decreases, the fitting constant should actually be larger. For larger Ω , the Si activation is smaller which is consistent with the results presented in Figure 6.3. For larger values of Ω' , the Se activation is larger

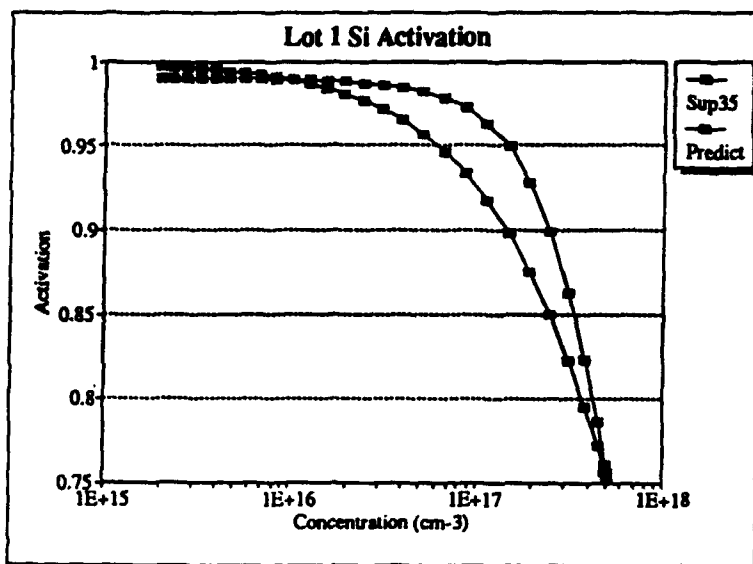


Figure 6.3: Fitting of Si Activation to Suprem3.5 Model. The value at the highest dopant density is fitted exactly.

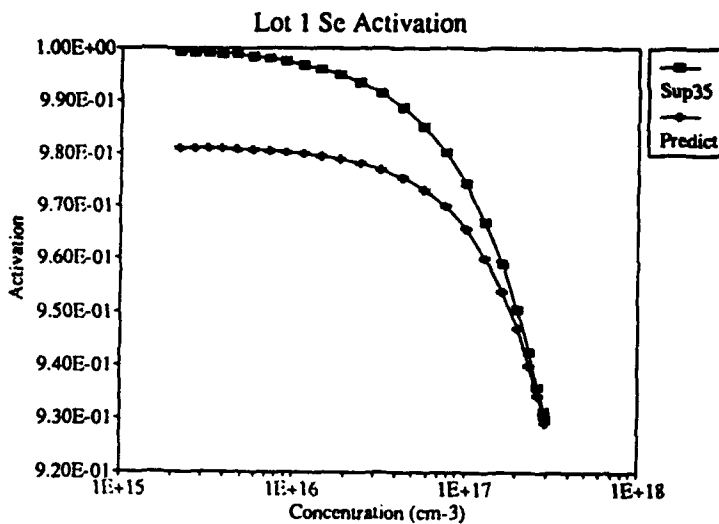


Figure 6.4: Fitting of Se Activation to Suprem3.5 Model. The value at the highest dopant density is fitted exactly.

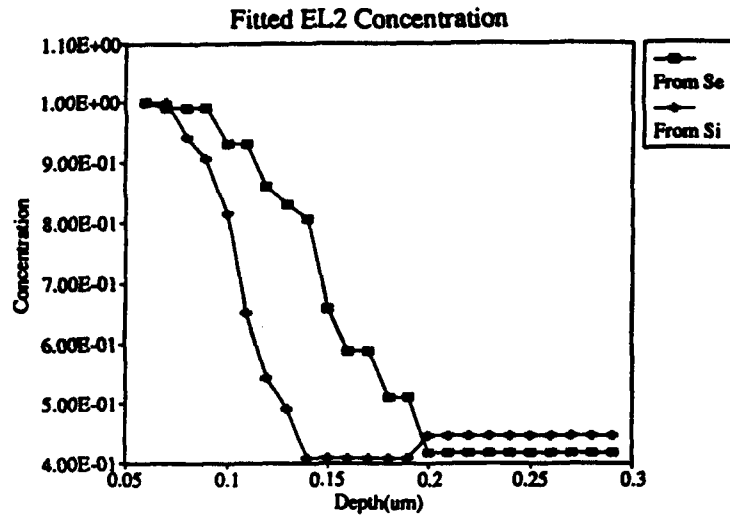


Figure 6.5: EL2 Concentration Resulting From the Fitting of Model Activation to Suprem3.5 Model.

which also is consistent with the results in Figure 6.4.

By varying the EL2 concentration, we may fit the Suprem3.5 activation calculations exactly. Figure 6.5 shows the resulting calculated EL2 concentrations. These data are again consistent with the experimental EL2 profiles obtained in [38, 39]. Although the profile obtained as a result of resulting from the fitting of the Si activation does not match that resulting from Se activation, they do bear a very remarkable resemblance. The final constant value for the EL2 concentration reached deep in the wafer obtained from the Si and Se activation profiles also match quite well.

Chapter 7

Short Channel Effects

The short channel effect results in a negative shift in the threshold voltage and lowering of the transconductance, causing degradation of MESFET performance. This effect is due fundamentally to the relationship between channel current and gate length. It can be seen even in the simplest constant mobility model of the MESFET in section 2.5.2. However, there are many more reasons for the short channel effect. Traditionally this effect in GaAs MESFETs is attributed to the gate to source and gate to drain resistances. The scaling of the gate lengths do not proportionally scale the source and drain resistances. As the gate lengths becomes very small, these resistances can have a dominant effect on device performance [40]. With the advent of self aligned gate technology, these resistance are much reduced. However, the roles of Carbon and EL2 in short channel effect has yet been fully explored.

7.1 The Role of Carbon and EL2

Let's first consider the simple P-N junction. The conduction and valence band diagram is shown in Figure 7.1. The built in voltage is given by:

$$V_{bi} = E_g - (V_n + V_p) \quad (7.1)$$

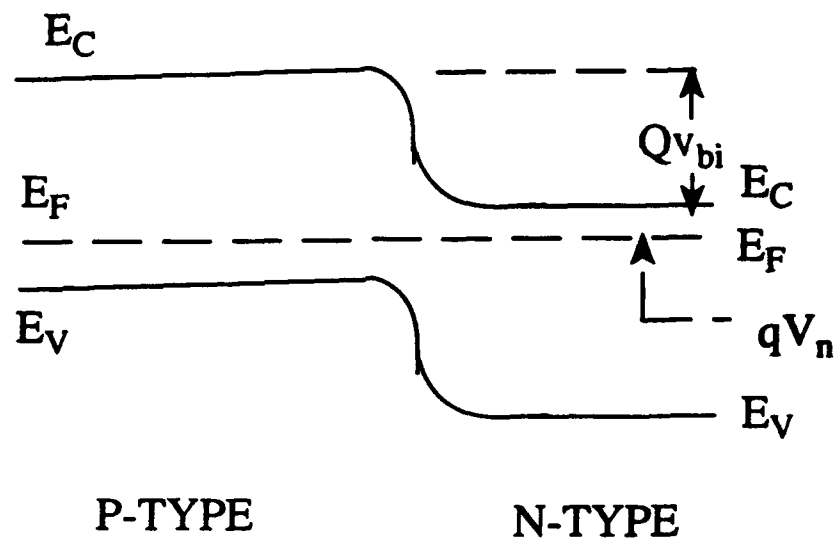


Figure 7.1: Fermi Level with Respect to the Conduction and Valence Band for Simple PN junction.

Let the depletion region width in the n-type side be x_n and p-type side be x_p . Then x_n and x_p are given by: [7]

$$x_n = \left[\frac{2\epsilon V_{bi} N_A}{q(N_D + N_A)N_D} \right]^{\frac{1}{2}} \quad (7.2)$$

The maximum electric field which occurs at the junction is given by:

$$\mathcal{E}_m = \frac{qN_D x_n}{\epsilon} = \frac{qN_A x_p}{\epsilon} \quad (7.3)$$

This field prevents the further drift of electrons from the n region into the p region.

Now suppose we add a deep donor to the p region whose concentration is above that of the p-type dopant. The region will now be semi-insulating. The conduction and valence band diagram for this case is shown in Figure 7.2. For this case, the electrons will flow from the n region into the semi-insulating region. In this process, some of the ionized deep donors become neutral leaving behind a net charge of ionized

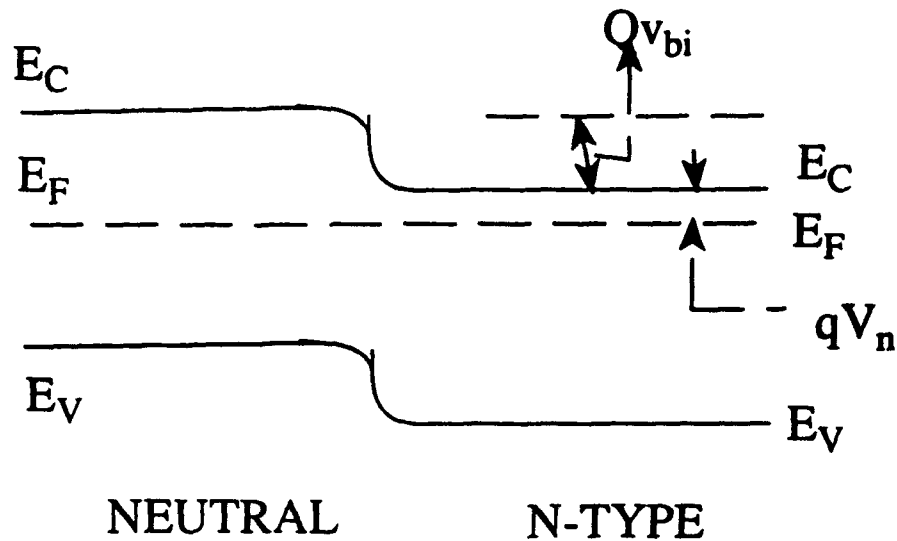


Figure 7.2: Fermi Level with Respect to the Conduction and Valence Band for Junction between n type and semi-insulating region.

acceptors. In this case, however the net N_A is much smaller than in the p-n junction case. For this situation, V_{bi} is reduced by approximately half the band gap. This causes the depletion width on the n side as well as the maximum field strength to be reduced.

This configuration is identical to the channel to substrate junction. In the presence of EL2, the depletion width is reduced when compared to the case of p-type substrate. This effectively increases the channel width. In addition, the reduced electric field at the junction makes it easier for energetic electrons to penetrate into the substrate and form a conduction path. Both of these factors contribute to an increase in the drain current, which in turn increases the threshold voltage of the device.

Figure 7.3 is a plot of threshold voltage as a function of EL2 concentration. Here the threshold voltages are calculated using the Medici simulation program, as are all subsequent electrical parameters. We see that the magnitude of the threshold voltage is only slightly dependent on the concentration of EL2, which is to be expected. Since EL2 concentration above the donor level is mostly neutral, these levels do not

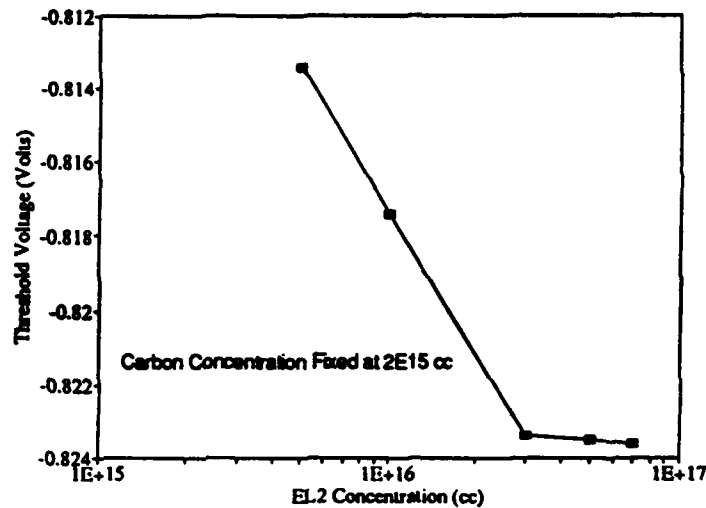


Figure 7.3: Threshold voltage as a function of EL2 concentration. The threshold voltages here is derived from Medici simulation.

contribute to current conduction. Only a small amount of conduction electrons arise from the EL2 donor increasing only slightly with increasing EL2 concentration.

Figure 7.4 shows threshold voltage calculated as a function of carbon concentration. The concentration of carbon is seen to effect the threshold voltage more than EL2 does. The concentration of carbon determines the metallurgical junction of the channel substrate junction. Higher carbon concentrations, the width of the channel is reduced which results in a reduction of channel current and threshold voltage. However as we see in Figures 4.1 and 4.2, the implanted dopant profile is extremely steep on the substrate side. So the channel width is only slightly dependent upon the carbon concentration for N_C near $5 \times 10^{15} \text{ cm}^{-3}$. This result is evident from inspecting figure 7.4.

Figure 7.5 shows the I-V characteristics of a MESFET calculated with and without EL2. It is evident that the presence of EL2 greatly increases the amount of current. As we discussed earlier, this effect is due to the reduction of the depletion width on the channel side when EL2 is present. In addition, current conduction in the substrate

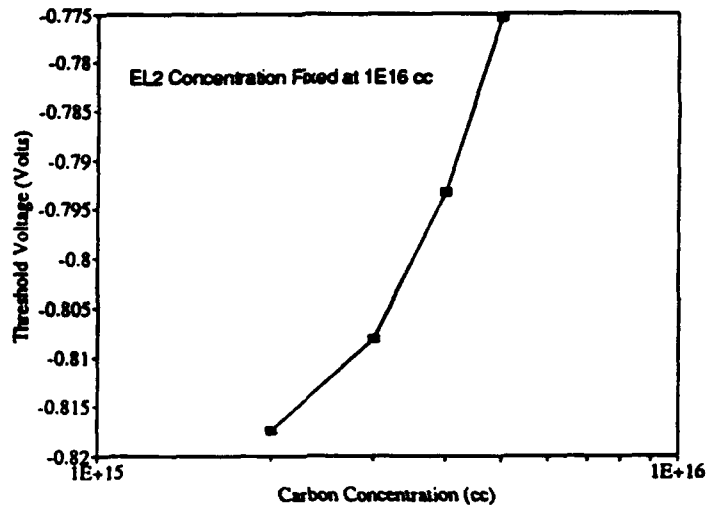


Figure 7.4: Threshold voltage as a function of carbon concentration. The threshold voltages here is derived from Medici simulation.

is also increased with EL2 present. This which results from the presence of EL2 reducing the potential barrier at the channel substrate interface, results in increased conduction current in the substrate. Figure 7.6 and 7.7, show vector diagrams of the conduction current in the channel as well as substrate, illustrate the above points.

7.2 Short Channel Effect

The short channel effect for self aligned gate structures is intimately connected to the amount of carbon and EL2 in the substrate region. As the gate length is shortened, the field in the channel is greatly increased with the same voltages applied to the gate and drain. The increased electric field causes increased injection of current into the substrate region, resulting in non-saturation of currents and leads to a more negative threshold voltage.

Figure 7.8 plots the experimentally measured threshold voltage vs gate length for Lot 1 Process structure. The predicted threshold voltages derived from Medici

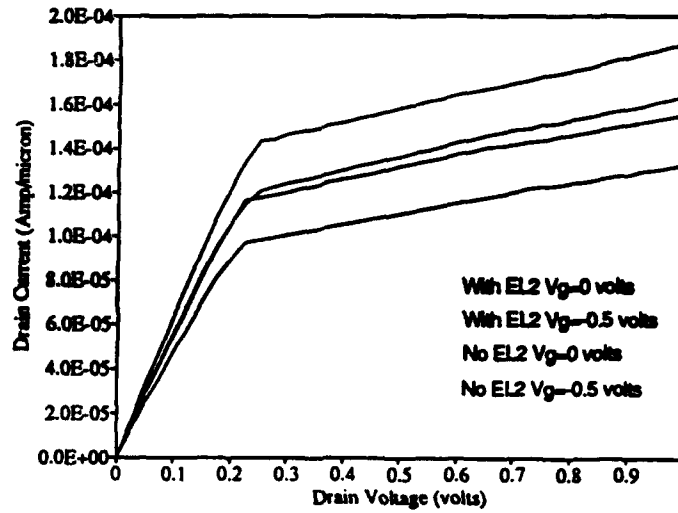


Figure 7.5: I-V characteristics of MESFET with and without deep donor EL2 in the substrate.

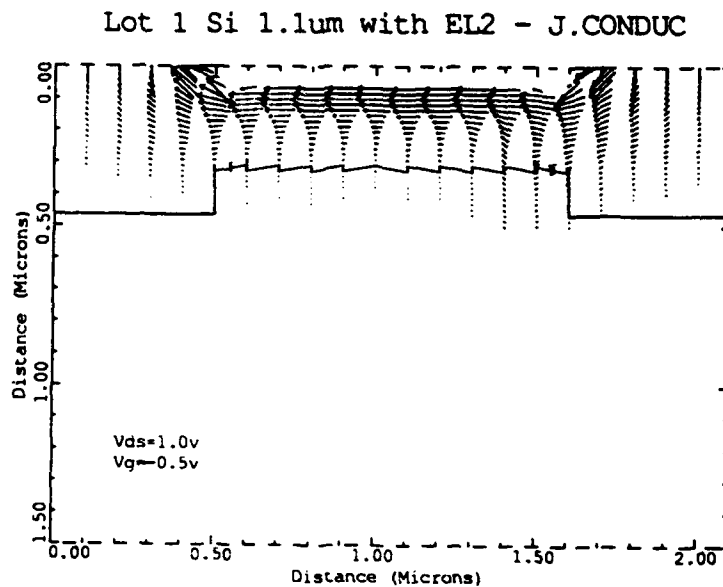


Figure 7.6: Vector Diagram of Conduction Current in a MESFET device. EL2 is set at $1 \times 10^{16} \text{ cm}^{-3}$ and Carbon level is at $2 \times 10^{15} \text{ cm}^{-3}$.

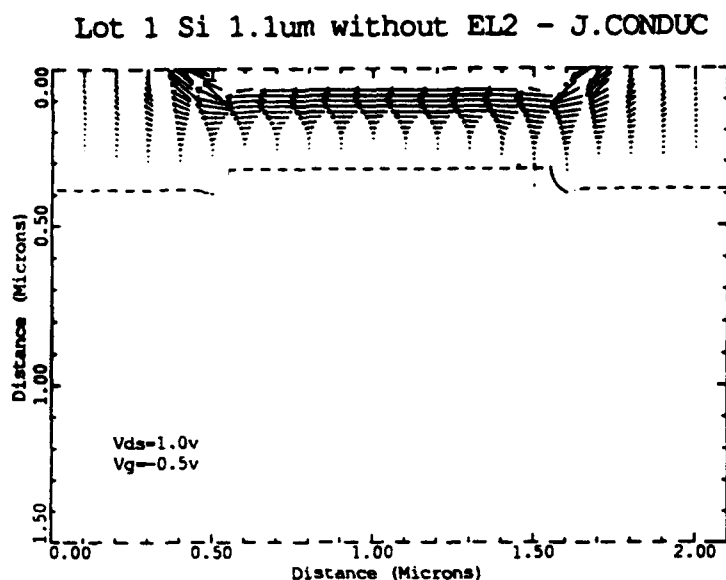


Figure 7.7: Vector Diagram of Conduction Current in a MESFET device. Carbon level is at $2 \times 10^{15} \text{ cm}^{-3}$. EL2 concentration is set to 0.

simulation is also shown. The gates of these devices are oriented in the [010] direction, which is 45 degrees from the major flat. As discussed in the next section, these directions are non-piezoelectric; therefore, can be used in study of short channel effects. The Medici output shows good agreement with the measured data.

Using the Medici simulator, Figure 7.9 and 7.10 are vector diagrams of the currents in our MESFET devices calculated. It is evident that at shorter channel lengths, the field between source and drain is increased for the same drain to source bias. This increased field causes increased current injection into the substrate. As a result, the current fails to saturate at larger V_g , for short channel devices.

As discussed in section 7.2, current injection into the substrate is reduced if the potential barrier at the channel-substrate interface is increased. This can be accomplished by increasing the p-type concentration in the substrate by ion implantation of a p-type dopant deep into the wafer near the channel-substrate interface.

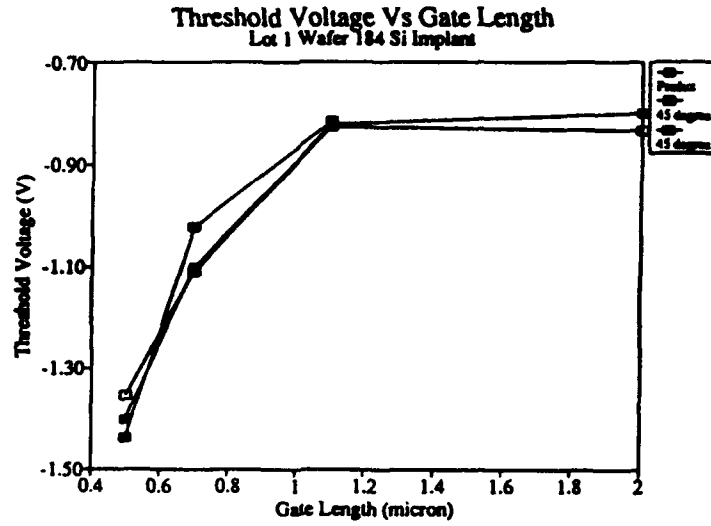


Figure 7.8: Threshold voltage as a function of gate length for MESFET devices. Medici simulation shows good agreement with experimental data.

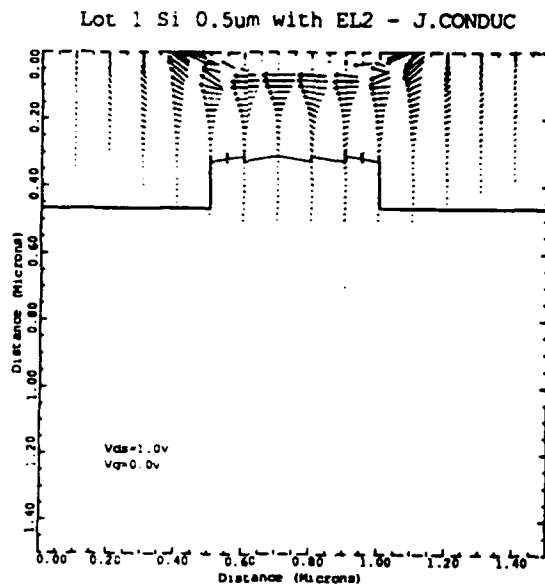


Figure 7.9: Vector diagram of conduction current for short gate MESFET.

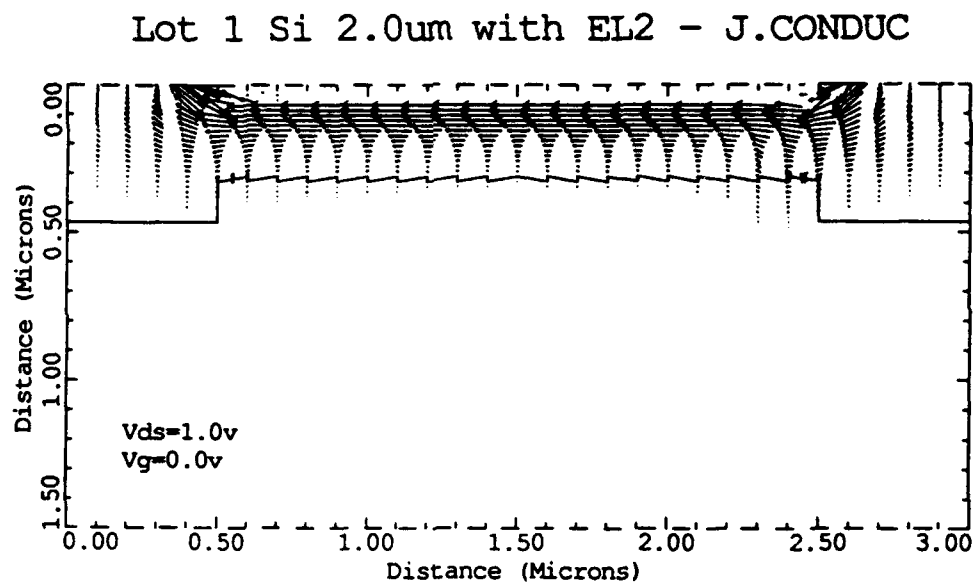


Figure 7.10: Vector diagram of conduction current for long gate MESFET.

Chapter 8

Piezoelectric Effect

It has long been known that the threshold voltage of a GaAs MESFET is dependent on the crystalline orientation of the gates. This is a problem unique to compound semiconductors. Because of the lack of centrosymmetry, when external pressure is applied to the lattice, ionic charge distortion occurs. This gives rise to a polarization vector which effectively adds a charge component to the channel.

8.1 Point Force Approximation

When thin films are deposited on the surface of GaAs during device fabrication, eg. Si_3N_4 , a stress σ_s results in the GaAs substrate. The stress is given by $\sigma_s = 4\sigma_f d_f / d_s$ [41], where σ_f is the overlayer dielectric film stress, and d_f and d_s are the thickness of the dielectric and semiconductor wafer, respectively. Since d_s is ordinarily much greater than d_f , the stress in the GaAs is much lower than that in the dielectric. However, when windows are opened up in the dielectric, such as for deposition of the Schottky gate metal, the stress imparted locally to the GaAs substrate from the edge of the dielectric film is greatly enhanced, approaching the stress value in the dielectric [41, 42].

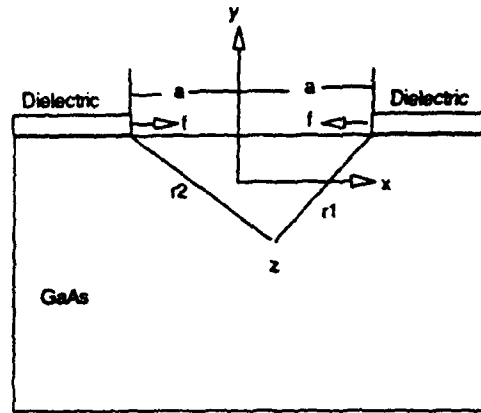


Figure 8.1: Schematic diagram of a GaAs FET used in the calculation of the stress distribution resulting from an opening in dielectric overlayer.

8.1.1 Stress Distribution

Consider the case shown in Figure 8.1, where a window is opened in the Si_3N_4 to deposit the gate metal. We wish to calculate the stress in the active channel resulting from the tangential stress component applied at the edge of the gate. Only the case of a wide gate FET is considered. In this approximation, the stress tensor does not depend on z , the FET width direction, by symmetry. This approximation is known as the "Plane Stress" case and can be solved analytically [43]. In the coordinate system defined in Figure 8.1, only σ_{xx} , σ_{yy} , σ_{zz} and $\sigma_{xy} = \sigma_{yx}$ are non-zero.

The stress tensor for the "Plane Stress" case may be solved as follows. If $N(t)$ and $T(t)$ are the normal and tangential stress applied to the boundary, where t is measured along the boundary, then:

$$\sigma_{xx} + \sigma_{yy} = 4R(\Phi(z)) \quad (8.1)$$

$$\sigma_{yy} - \sigma_{xx} + 2i\sigma_{xy} = 2(\overline{z}\Phi'(z) + \Psi(z)) \quad (8.2)$$

Where z is a complex variable given by $x+iy$ and Φ and Ψ are given by:

$$\Phi = -\frac{1}{2\pi i} \int_{-\infty}^{\infty} \frac{N - iT}{t - z} dt \quad (8.3)$$

$$\Psi = -\frac{1}{2\pi i} \int_{-\infty}^{\infty} \frac{N + iT}{t - z} dt + \frac{1}{2\pi i} \int_{-\infty}^{\infty} \frac{N - iT}{(t - z)^2} t dt \quad (8.4)$$

The following symbols are defined for our calculation: $x_1 = x - a$, $x_2 = x + a$, $z = x + iy$, $z_1 = x_1 + iy$ and $z_2 = x_2 + iy$. In our case, $N(t) = 0$ and $T(t) = \sigma$ at $x = \pm a$ and $T(t) = 0$ otherwise.

$$\begin{aligned} \Phi(z) &= \frac{1}{2\pi} \int_{-\infty}^{\infty} \frac{T}{t - z} dt \\ &= \frac{\sigma}{2\pi} \left[\int_{-a-\delta}^{-a+\delta} \frac{dt}{t - z} - \int_{a-\delta}^{a+\delta} \frac{dt}{t - z} \right] \end{aligned} \quad (8.5)$$

The integrals are evaluated by keeping $\sigma\delta = f = \text{constant}$ and lettering $\delta \rightarrow 0$. In that limit, we obtain:

$$\Phi(z) = \frac{f}{\pi} \left(\frac{1}{z_1} - \frac{1}{z_2} \right) \quad (8.6)$$

$$\Psi(z) = -2\Phi(z) - z\Phi'(z) \quad (8.7)$$

and

$$\sigma_{xx} = \frac{4fd}{\pi} \left(\frac{x_1^3}{r_1^4} - \frac{x_2^3}{r_2^4} \right) \quad (8.8)$$

$$\sigma_{yy} = \frac{4fd}{\pi} \left(\frac{x_1 y^2}{r_1^4} - \frac{x_2 y^2}{r_2^4} \right) \quad (8.9)$$

$$\sigma_{zz} = \nu(\sigma_{xx} + \sigma_{yy}) = \frac{4f\nu}{\pi} \left(\frac{x_1}{r_1^2} - \frac{x_2}{r_2^2} \right) \quad (8.10)$$

$$\sigma_{xy} = \sigma_{yx} = \frac{4f}{\pi} \left(\frac{yx_1^2}{r_1^4} - \frac{yx_2^2}{r_2^4} \right) \quad (8.11)$$

where ν is the Poisson's ratio and has a value of 0.23 for GaAs [41].

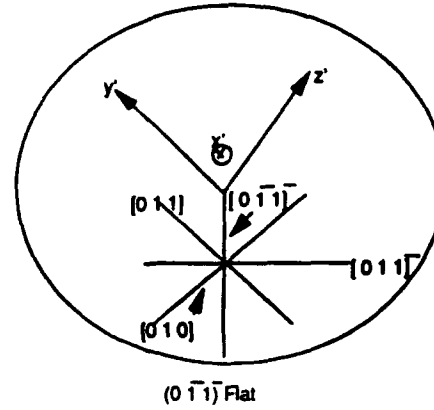


Figure 8.2: Schematic diagram illustrating the orientation of the coordinate system used in this calculation and that of the MESFETs.

8.1.2 Effective Charge Calculation

We shall now transform our coordinate system for the specific calculation for (100) oriented wafers. We shall use a coordinate system with the y-axis oriented along the gate length and x-axis pointing from the gate downward into the substrate. The coordinate configuration is shown in Fig. 8.2. In this coordinate system, the stress tensor is given by:

$$\sigma_1 = \sigma_{xx} = \frac{4f_d}{\pi} \left(\frac{y_1 x^2}{r_1^4} - \frac{y_2 x^2}{r_2^4} \right) \quad (8.12)$$

$$\sigma_2 = \sigma_{yy} = \frac{4f_d}{\pi} \left(\frac{y_1^3}{r_1^4} - \frac{y_2^3}{r_2^4} \right) \quad (8.13)$$

$$\sigma_3 = \sigma_{zz} = \frac{4f_d \nu}{\pi} \left(\frac{y_1}{r_1^2} - \frac{y_2}{r_2^2} \right) \quad (8.14)$$

$$\sigma_6 = \sigma_{xy} = \sigma_{yx} = \frac{4f_d}{\pi} \left(\frac{xy_1^2}{r_1^4} - \frac{xy_2^2}{r_2^4} \right) \quad (8.15)$$

The piezoelectric tensor is a tensor of rank three which relates the polarization vector to the stress tensor. Since its second and third indices are symmetric, it may be reduced to a two index form according to the following rule: [44]

$$\begin{array}{l} \text{tensor notation} \quad 11 \quad 22 \quad 33 \quad 23,32 \quad 31,13 \quad 12,21 \\ \text{matrix notation} \quad 1 \quad 2 \quad 3 \quad 4 \quad 5 \quad 6 \end{array} \quad (8.16)$$

In this new matrix notation, we define $d_{ij}=d_{imm}$ and $d_{ij}=2d_{imn}$ where $m \neq n$. Both mm and mn above transform to j according to our contraction rule. Using the same method, the second ranked stress tensor is transformed to the one index notation with $\sigma_i = \sigma_{jk}$. With these definitions, the polarization vector may finally be written as:

$$P_i = \sum_{j=1}^6 d_{ij} \sigma_j \quad (8.17)$$

Our wafers are all (100) oriented with their major flat on the $(0\bar{1}\bar{1})$ surface. The devices are fabricated at 0, +45, -45 and 90 degrees to the major flat, corresponding to the $[01\bar{1}]$, $[010]$, $[0\bar{1}\bar{1}]$ and $[001]$ directions as shown in Figure 8.2. For the $x'y'z'$ coordinate system shown, the only non-zero components of the piezoelectric tensor are $d_{14}=d_{25}=d_{36}=d$. In computing the polarization vector, we set up our coordinate system such that the y-axis is parallel to the direction of the gate length and the x-axis points downward from the gate into the substrate. Since this is the coordinate system in which our stress tensors are expressed, we must, therefore transform our piezoelectric tensor into this system.

(1) $[01\bar{1}]$ oriented devices parallel to the major flat.

The new coordinate system will be $x=[100]$, $y=[0\bar{1}\bar{1}]/\sqrt{2}$, $z=[01\bar{1}]/\sqrt{2}$.

So the transformation matrix is:

$$a = \begin{pmatrix} 1 & 0 & 0 \\ 0 & -\frac{1}{\sqrt{2}} & \frac{1}{\sqrt{2}} \\ 0 & -\frac{1}{\sqrt{2}} & -\frac{1}{\sqrt{2}} \end{pmatrix} \quad (8.18)$$

The piezoelectric tensor transforms as a tensor of rank three and is given by:

$$d_{ijk} = a_{il}a_{jm}a_{kn}d'_{lmn} \quad (8.19)$$

In this coordinate system, we obtain:

$$d_{12} = d_{122} = -d/2, \quad d_{13} = d_{133} = d/2$$

$$d_{26} = 2d_{212} = -d, \quad d_{35} = 2d_{313} = d$$

The resulting polarization vector is:

$$\begin{aligned} P_1 &= \frac{d}{2}(\sigma_3 - \sigma_2) \\ &= \frac{2f_d d}{\pi} \left(\nu \left(\frac{y_1}{r_1^2} - \frac{y_2}{r_2^2} \right) - \left(\frac{y_1^3}{r_1^4} - \frac{y_2^3}{r_2^4} \right) \right) \end{aligned} \quad (8.20)$$

$$P_2 = -d\sigma_6 = -\frac{4f_d d}{\pi} \left(\frac{xy_1^2}{r_1^4} - \frac{xy_2^2}{r_2^4} \right) \quad (8.21)$$

$$P_3 = d\sigma_5 = 0 \quad (8.22)$$

The polarization can be turned into an effective polarization charge as $\rho = -\nabla \cdot P$. We finally obtain:

$$\rho = \frac{4f_d d}{\pi} \left(\frac{2xy_1}{r_1^4} - \frac{6xy_1^3}{r_1^6} + \frac{2xy_2}{r_2^4} - \frac{6xy_2^3}{r_2^6} + \nu \left(\frac{xy_1}{r_1^4} - \frac{xy_2}{r_2^4} \right) \right) \quad (8.23)$$

(2) $[0\bar{1}\bar{1}]$ oriented devices perpendicular to the major flat.

Here the new coordinate system is $x=[100]$, $y=[011]/\sqrt{2}$, $z=[0\bar{1}\bar{1}]/\sqrt{2}$. The resulting transformation matrix is:

$$a = \begin{pmatrix} 1 & 0 & 0 \\ 0 & \frac{1}{\sqrt{2}} & \frac{1}{\sqrt{2}} \\ 0 & -\frac{1}{\sqrt{2}} & \frac{1}{\sqrt{2}} \end{pmatrix} \quad (8.24)$$

In this coordinate system, we obtain:

$$d_{12} = d_{122} = -d/2, \quad d_{13} = d_{123} = -d/2$$

$$d_{26} = 2d_{212} = d, \quad d_{35} = 2d_{313} = -d$$

As we can see, these piezoelectric tensor components have exactly the same magnitude as in the previous case, but have the opposite sign. Therefore, the effective polarization charge will have the opposite sign.

(3) [010] oriented devices at 45 degree to the major flat.

The new coordinate system is $x=[100]$, $y=[001]$, $z=[0\bar{1}0]$, and the resulting transformation matrix is:

$$a = \begin{pmatrix} 1 & 0 & 0 \\ 0 & 0 & 1 \\ 0 & -1 & 0 \end{pmatrix} \quad (8.25)$$

As a result, $d_{14}=d_{25}=d_{36} = -d$. So only the z-component of the polarization vector is non-zero, given by $-d\sigma_6$. Since all the stress tensors are independent of z, the effective charge will be zero.

The case where devices are oriented at -45 degree to the major flat can be similarly calculated and the effective polarization charge is zero as expected.

8.2 Gaussian Force Approximation

As we see in the point force approximation, the effective charge distribution is singular at the points where the forces are exerted. This is to be expected for a point force. Because of singularities; however, the point force approximation is not suitable for device simulation. In addition, in real situation, any force must be exerted over a finite extent. Therefore, we shall use a Gaussian approximation where the forces are centered at the edge of the window opening and fall off as a Gaussian towards both sides.

We shall once again start with equation 8.3 and 8.4.

$$\begin{aligned}\Phi(z) &= \frac{1}{2\pi} \int_{-\infty}^{\infty} \frac{T(t)}{t-z} dt \\ &= \frac{1}{2\pi} \int_{-\infty}^{\infty} \frac{T(t)(t-x+iy)}{(t-x)^2+y^2} dt\end{aligned}\quad (8.26)$$

$$\Rightarrow \operatorname{Re}(\Phi(z)) = \frac{1}{2\pi} \int_{-\infty}^{\infty} \frac{T(t)(t-x)}{(t-x)^2+y^2} dt \quad (8.27)$$

$$\operatorname{Im}(\Phi(z)) = \frac{1}{2\pi} \int_{-\infty}^{\infty} \frac{T(t)y}{(t-x)^2+y^2} dt \quad (8.28)$$

$$\begin{aligned}\Psi(z) &= -\frac{1}{2\pi} \int_{-\infty}^{\infty} \frac{T(t)}{t-z} dt - \Phi(z) - z\Phi'(z) \\ &= -2\Phi(z) - z\Phi'(z)\end{aligned}\quad (8.29)$$

$$\begin{aligned}\Phi'(z) &= \frac{1}{2\pi} \int_{-\infty}^{\infty} \frac{T(t)}{(t-z)^2} dt \\ &= \frac{1}{2\pi} \int_{-\infty}^{\infty} \frac{T(t)((t-x)^2-y^2+i2(t-x)y)}{((t-x)^2+y^2)^2} dt\end{aligned}\quad (8.30)$$

$$\Rightarrow \operatorname{Re}(\Phi'(z)) = \frac{1}{2\pi} \int_{-\infty}^{\infty} \frac{T(t)((t-x)^2-y^2)}{((t-x)^2+y^2)^2} dt \quad (8.31)$$

$$\operatorname{Im}(\Phi'(z)) = \frac{1}{2\pi} \int_{-\infty}^{\infty} \frac{T(t)(2(t-x)y)}{((t-x)^2+y^2)^2} dt \quad (8.32)$$

With the above setup, we obtain:

$$\sigma_{yy} = 2y \operatorname{Im}(\Phi')$$

$$\sigma_{xx} = 4 \operatorname{Re}(\Phi) - 2y \operatorname{Im}(\Phi')$$

$$\sigma_{xy} = \sigma_{yx} = -2y \operatorname{Re}(\Phi') - 2 \operatorname{Im}(\Phi)$$

$$\sigma_{zz} = \nu(\sigma_{xx} + \sigma_{yy})$$

where ν is 0.23 for GaAs.

To calculate the effective charge concentration, we again re-orient our coordinates as shown in Figure 8.2. The procedure is exactly the same as section 8.1. For the $[01\bar{1}]$ oriented FET, we obtain:

$$\rho(x, y) = M \int_{-\infty}^{\infty} T(t) \left(\frac{6x(t-y)^3}{((t-y)^2 + x^2)^3} - \frac{(\nu + 2)x(t-y)}{((t-y)^2 + x^2)^2} \right) dt$$

where M is a fitting constant. $T(t)$ here is a general force and will be treated as Gaussian in subsequent simulation.

It's worth noting that if the point force approximation is used in any of the general formula derived above, we arrive at exactly the same result as obtained in section 8.1.

8.3 Discussion

We write the Gaussian force as:

$$T = H \exp \left[-\left(\frac{t+a}{\sigma} \right)^2 \right] - H \exp \left[-\left(\frac{t-a}{\sigma} \right)^2 \right] \quad (8.33)$$

where the constant H can of course be absorbed into the overall fitting constant.

Figure 8.3, 8.4 and 8.5 shows the piezoelectric charge distribution in the channel of the MESFET obtained by numerical integration. The graphs are symmetric with respect to the center of the gate as expected. The charges are highly peaked around the peak of the force.

Figures 8.6 and 8.7 constructed from experimental data taken from Lot 2 confirm our calculations. The threshold voltages here are wafer scale averages. We notice that the V_t increased for the ± 45 degree oriented FETs have nearly identical threshold voltages, while the 0 and 90 degree oriented FETs are split on the opposite sides of the 45 degree FETs. These results confirm that ± 45 degree orientation are the non-piezoelectric orientations and that the 0 and 90 degree orientations exhibit opposite piezoelectric effects. The gate length dependence of the 45 degree FETs result solely

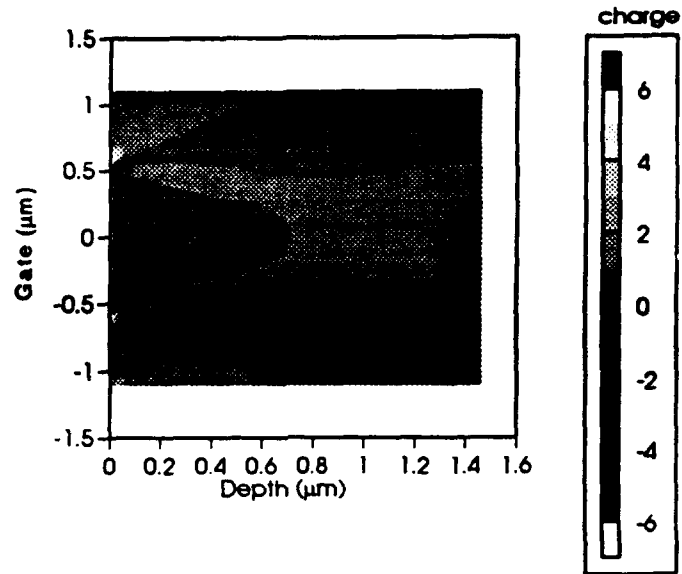


Figure 8.3: Charge distribution in the channel due to piezoelectric effect. Gaussian force approximation for $1.1\mu\text{m}$ device, $\sigma = 0.01\mu\text{m}$.

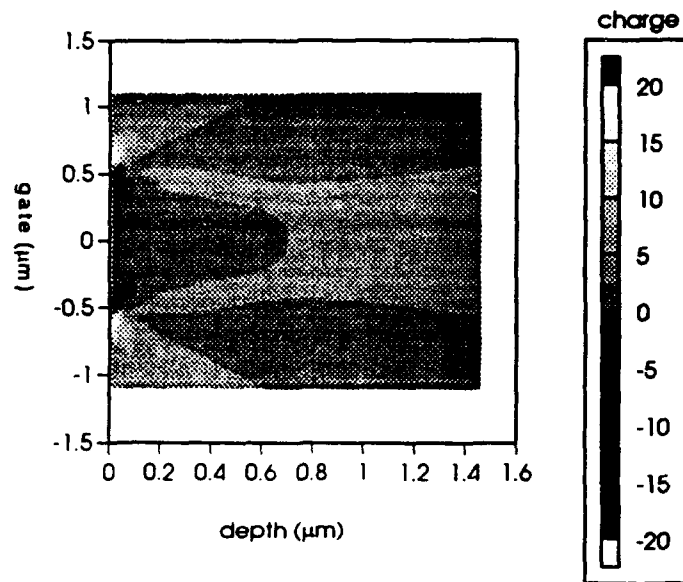


Figure 8.4: Charge distribution in the channel due to piezoelectric effect. Gaussian force approximation for $1.1\mu\text{m}$ device, $\sigma = 0.1\mu\text{m}$.

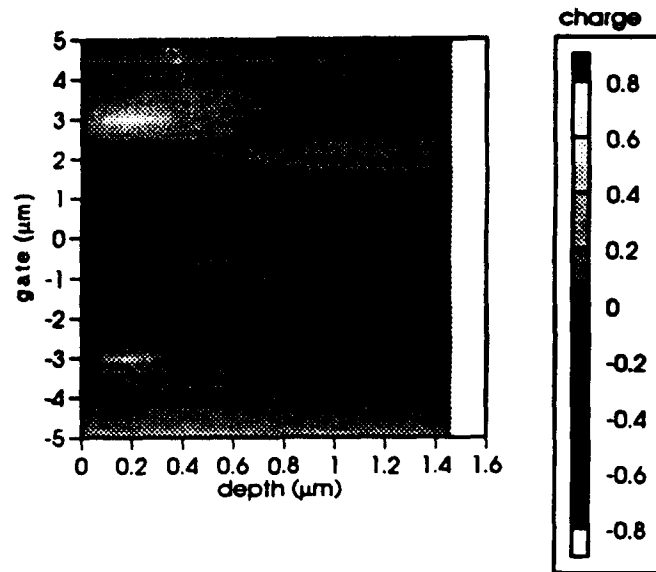


Figure 8.5: Charge distribution in the channel due to piezoelectric effect. Gaussian force approximation for $5.0\mu\text{m}$ device, $\sigma = 0.1\mu\text{m}$.

by short channel effects while a combination of short channel and piezoelectric effects are responsible for the 0 and 90 degree oriented FET gate length dependence.

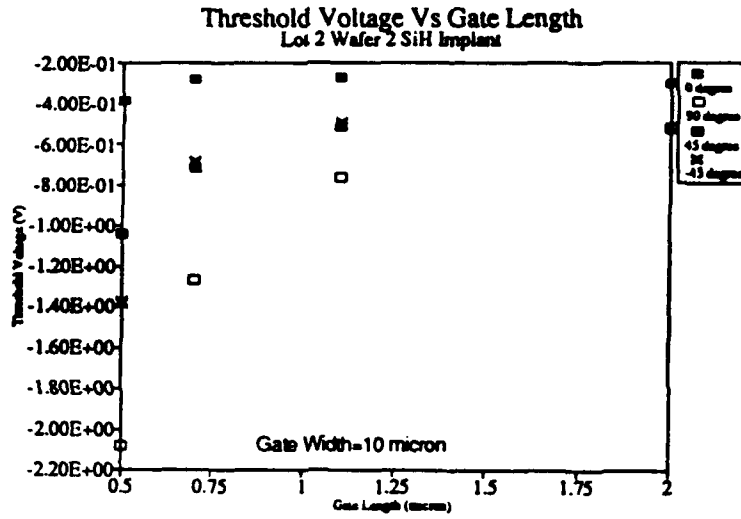


Figure 8.6: Piezoelectric shift of the threshold voltage for Si channel implanted devices.

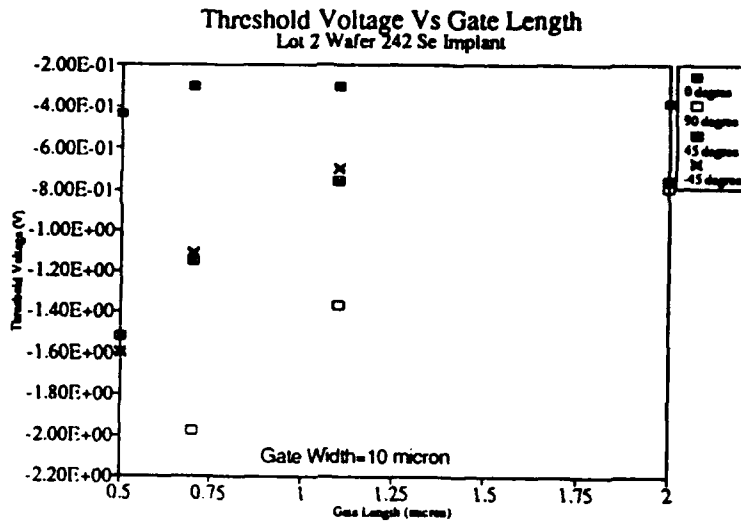


Figure 8.7: Piezoelectric shift of the threshold voltage for Se channel implanted devices.

Chapter 9

Conclusions

The purpose of this study is to understand the electrical properties of GaAs MESFETs in relationship to the physical structure of the device and the defect structure of the substrate. We focused on three issues. Firstly, the equilibrium properties of GaAs containing implanted species such as Si and Se. We took into account in this analysis the As anti-site defect known as EL2 and developed models for the activation of Si and Se in GaAs. Secondly, we studied the effect of short channels on GaAs MESFETs. We found again that EL2 and carbon doping play a crucial role. Thirdly, we investigated the orientation dependence of the electric characteristics of GaAs MESFETs known as the piezoelectric effect. We were able to derive an equation for an effective charge based on the principles of elasticity.

Dopant activation of Si and Se implants in GaAs is an extremely important issue. Understanding the activation processes well go a long way to explain reasons for the threshold voltage fluctuations in GaAs MESFETs. Manufacturing yields are a problem which plagues the GaAs IC industry. Low yields greatly increase the cost of integrated circuits. By understanding and improving threshold voltage uniformity, we can not only improve yields, but also increase the level and scale of integration.

With a combination of experimental measurement and the theoretical models developed here, we can greatly improve existing process modeling software to derive the amount of activation as well as understand the physical mechanisms controlling activation. By understanding these mechanisms, we improve our ability to develop

processes that meet the demand for fabrication of GaAs ICs of increased sophistication and complexity.

In our study, we point out the shortcomings of previous activation models. In our derivation, we show that EL2, the deep donor, plays a crucial role in the activation of both Si as well as Se in GaAs. We believe that this model is consistent with all reported threshold voltage fluctuation data as well as EL2 distribution mappings.

Short channel effects are another issue effecting the development processes for large scale integration processes for GaAs ICs. For submicron gate length devices, the short channel effect seriously degrades the performance of MESFETs and must be understood and dealt with if high performance and large scale integration are to be achieved. We show through detailed simulation that the ion implantation of a p-type buffer layer is useful in reducing short channel effects.

The piezoelectric effect is unique to compound semi-conductors. We derive an equation based on the principles of elasticity to account for this effect. By using a Gaussian force centered around the edge of the gate dielectric, the piezoelectric effect can be effectively modeled using a two dimensional simulator.

We believe further studies are needed especially in the area of Si and Se activation in GaAs. We need to systematically understand the distribution of various point defects in GaAs. Experimental efforts are needed to map the lateral as well as depth profile of these defects.

Appendix A

Stress Calculation

Let's follow the notation outlined in chapter 8. We will assume a point force applied at the edge of the gate as shown in Figure 8.1.

$$\begin{aligned}\Phi &= -\frac{1}{2\pi i} \int_{-\infty}^{\infty} \frac{N - iT}{t - z} dt \\ &= \frac{1}{2\pi} \int_{-\infty}^{\infty} \frac{T}{t - z} dt \\ &= \frac{\sigma}{2\pi} \left[\int_{-a-\delta}^{-a+\delta} \frac{dt}{t - z} - \int_{a-\delta}^{a+\delta} \frac{dt}{t - z} \right] \\ &= \frac{\sigma}{2\pi} [\ln(a - \delta + z) - \ln(a + \delta + z) - \ln(a + \delta - z) + \ln(a - \delta - z)]\end{aligned}$$

By neglecting high order of δ , we obtain:

$$\Phi = \frac{\sigma\delta}{2\pi} \left(\frac{2}{z_1} - \frac{2}{z_2} \right) = \frac{f_d}{\pi} \left(\frac{1}{z_1} - \frac{1}{z_2} \right) \quad (\text{A.1})$$

$$z_1 = r_1 \exp(i\theta_1) \quad z_2 = r_2 \exp(i\theta_2) \quad (\text{A.2})$$

$$\begin{aligned}\sigma_{xx} + \sigma_{yy} &= 4\text{Re}[\Phi(z)] \\ &= \frac{4f_d}{\pi} \text{Re} \left(\frac{\exp(-i\theta_1)}{r_1} - \frac{\exp(-i\theta_2)}{r_2} \right)\end{aligned} \quad (\text{A.3})$$

$$\begin{aligned}
\Psi &= -\frac{1}{2\pi i} \int_{-\infty}^{\infty} \frac{N + iT}{t - z} dt - \Phi(z) - z\Phi'(z) & (A.4) \\
&= -\frac{1}{2\pi} \int_{-\infty}^{\infty} \frac{T}{t - z} dt - \Phi(z) - z\Phi'(z) \\
&= -2\Phi(z) - z\Phi'(z)
\end{aligned}$$

$$\bar{z}\Phi'(z) + \Psi(z) = -2\Phi(z) + (\bar{z} - z)\Phi'(z) \quad (A.5)$$

$$\begin{aligned}
&= -2\frac{f_d}{\pi} \left(\frac{\exp(-i\theta_1)}{r_1} - \frac{\exp(-i\theta_2)}{r_2} \right) - 2iy\frac{f_d}{\pi} \left(-\frac{1}{z_1^2} + \frac{1}{z_2^2} \right) \\
&= -\frac{2f_d}{\pi} \left[\frac{\exp(-i\theta_1)}{r_1} - \frac{\exp(-i\theta_2)}{r_2} \right. \\
&\quad \left. + iy \left(-\frac{\exp(-2i\theta_1)}{r_1^2} + \frac{\exp(-2i\theta_2)}{r_2^2} \right) \right] & (A.6)
\end{aligned}$$

$$\sigma_{xy} = \text{Im}[\bar{z}\Phi'(z) + \Psi(z)] \quad (A.7)$$

$$\begin{aligned}
&= -\frac{2f_d}{\pi} \left[-\frac{\sin\theta_1}{r_1} + \frac{\sin\theta_2}{r_2} + y \left(-\frac{\cos 2\theta_1}{r_1^2} + \frac{\cos 2\theta_2}{r_2^2} \right) \right] \\
&= \frac{2f_d}{\pi} \left(\frac{\sin\theta_1 + \sin\theta_1 \cos 2\theta_1}{r_1} - \frac{\sin\theta_2 + \sin\theta_2 \cos 2\theta_2}{r_2} \right) \\
&= \frac{2f_d}{\pi} \left(\frac{\sin\theta_1 \cdot 2\cos^2\theta_1}{r_1} - \frac{\sin\theta_2 \cdot 2\cos^2\theta_2}{r_2} \right) \\
&= \frac{4f_d}{\pi} \left(\frac{yx_1^2}{r_1^4} - \frac{yx_2^2}{r_2^4} \right) & (A.8)
\end{aligned}$$

$$\begin{aligned}
\sigma_{yy} - \sigma_{xx} &= 2\text{Re}[\bar{z}\Phi'(z) + \Psi(z)] \\
&= 2\text{Re}[-2\Phi(z) + (\bar{z} - z)\Phi'(z)] & (A.9)
\end{aligned}$$

$$\sigma_{yy} + \sigma_{xx} = 4\text{Re}[\Phi(z)] \quad (A.10)$$

$$\Rightarrow 2\sigma_{yy} = 2\text{Re}[(\bar{z} - z)\Phi'(z)]$$

$$\begin{aligned}\sigma_{yy} &= -\frac{2f_d y}{\pi} \left(-\frac{\sin 2\theta_1}{r_1^2} + \frac{\sin 2\theta_2}{r_2^2} \right) \\ &= \frac{4f_d}{\pi} \left(\frac{x_1 y^2}{r_1^4} - \frac{x_2 y^2}{r_2^4} \right)\end{aligned}\quad (\text{A.11})$$

$$\begin{aligned}\sigma_{xx} &= \frac{4f_d}{\pi} \left(\frac{\cos \theta_1}{r_1} - \frac{\cos \theta_2}{r_2} - \frac{x_1 y^2}{r_1^4} + \frac{x_2 y^2}{r_2^4} \right) \\ &= \frac{4f_d}{\pi} \left(\frac{x_1(r_1^2 - y^2)}{r_1^4} - \frac{x_2(r_2^2 - y^2)}{r_2^4} \right) \\ &= \frac{4f_d}{\pi} \left(\frac{x_1^3}{r_1^4} - \frac{x_2^3}{r_2^4} \right)\end{aligned}\quad (\text{A.12})$$

$$\sigma_{zz} = \gamma(\sigma_{xx} + \sigma_{yy}) \quad (\text{A.13})$$

$$\begin{aligned}&= \frac{4f_d \gamma}{\pi} \left(\frac{x_1^3 + x_1 y^2}{r_1^4} - \frac{x_2^3 + x_2 y^2}{r_2^4} \right) \\ &= \frac{4f_d \gamma}{\pi} \left(\frac{x_1}{r_1^2} - \frac{x_2}{r_2^2} \right)\end{aligned}\quad (\text{A.14})$$

So in summary, the stress distribution in the channel due to point forces applied at the edge of the gate is given by:

$$\sigma_{xx} = \frac{4f_d}{\pi} \left(\frac{x_1^3}{r_1^4} - \frac{x_2^3}{r_2^4} \right) \quad (\text{A.15})$$

$$\sigma_{yy} = \frac{4f_d}{\pi} \left(\frac{x_1 y^2}{r_1^4} - \frac{x_2 y^2}{r_2^4} \right) \quad (\text{A.16})$$

$$\sigma_{zz} = \frac{4f_d \gamma}{\pi} \left(\frac{x_1}{r_1^2} - \frac{x_2}{r_2^2} \right) \quad (\text{A.17})$$

$$\sigma_{xy} = \sigma_{yx} = \frac{4f_d}{\pi} \left(\frac{y x_1^2}{r_1^4} - \frac{y x_2^2}{r_2^4} \right) \quad (\text{A.18})$$

Bibliography

- [1] Raph Williams, "Modern GaAs Processing Methods," 2nd Ed., Artech, 1990.
- [2] J. S. Blakemore, "Semiconducting and Other Major Properties of Gallium Arsenide," J. Appl. Phys. 53(10), October 1982.
- [3] S. J. Pearton, "Ion Implantation in GaAs," Solid State Phenomena Vol. 1&2 (1988) pp. 247-280.
- [4] P. A. Markowich, C. A. Ringhofer, C. Schmeiser, "Semiconductor Equations," Springer-Verlag, 1990.
- [5] Siegfried Selberherr, "Analysis and Simulation of Semiconductor Devices," Springer-Verlag, 1984.
- [6] S. M. Sze, "Physics of Semiconductor Devices," 2nd Edition, Wiley, 1981.
- [7] Sandip Tiwari, "Compound Semiconductor Device Physics," Academic Press 1992.
- [8] Mark R. Pinto, Conor S. Rafferty and Robert W. Dutton, "PISCES-II User's Manual," Stanford Electronics Laboratories, Department of Electrical Engineering, Stanford University 1984.
- [9] "Medici, Two Dimensional Device Simulation Program," Technology Modeling Associates, Inc 1993.
- [10] Mircea A, Mitonneau A, Hollan L, and Briere A, Appl. Phys. 11, 153, 1976.

- [11] S. Makram-Ebeid, P. Langlade and G.M. Martin in *Semi-insulating III-V Materials: Kah-Nee-Ta*, p182, 1984.
- [12] G.P.Li and K.L.Wang, *J. appl. Phys.* 53, 8653,1982.
- [13] M. Baeumler, U. Kaufmann, and J. Windscheif. *Appl. Phys. Letters* 46, 781, 1985.
- [14] M. O. Manasreh, D. W. Fischer, and W.C. Mitchel, *Phys. Stat. Sol. (b)* 154, 11, 10, 1984.
- [15] G. B. Bachelet and M. Scheffler. *Proc. 17th Internat. Conf. Phys. Semicond.* 1984.
- [16] J. Jimenez, P. Hernandez, J.A. DeSaja, and J. Bonnafa, *Solid State Commun.* 55, 459, 1985.
- [17] P. Dobrilla and J.S. Blakemore, *J. Appl. Phys.* 58(1) 208, 1985.
- [18] A. Chantre, G. Vincent, and D. Bois, *Phys. Rev. B*23, 5335, 1981.
- [19] P. Silverberg, P. Omling, and L. Samuelson, *Appl. Phys. Lett.* 52 (20), 1689, 1988.
- [20] J.S. Blakemore, L. Sargent, and R.S. Tang, *Appl. Phys. Lett.* 54 (21) 2106, 1989.
- [21] Michio Tajima, *J. of Crystal Growth*, 103, 1, 1990.
- [22] Michio Tajima, *Appl. Phys. Lett.* 53 (11), 959, 1988.
- [23] P. Dobrilla and J.S. Blakemore, *Appl. Phys. Lett.* 47 (6), 602, 1985.
- [24] Shintaro Miyazawa and Kazumi Wada, *Appl. Phys. Lett.* 48 (14) 487, 1986.
- [25] J. P. Fillard, P. Gall, A. Baroudi and J. Bonnafe, "Short Range Association of EL2 with Dislocations in GaAs-In Materials," *Solid State Communications*, Vol.,67, No. 3. pp. 321-323, 1988.
- [26] Richard A. Swalin, "Thermodynamics of Solids," Second Edition, Wiley, 1972.

- [27] F. A. Kröger, "The Chemistry of Imperfect Crystals," 2nd Edition, North Holland, 1974.
- [28] F. A. Kröger and H. J. Vink, "Relations Between the Concentrations of Imperfections in Crystalline Solids," in Solid State Physics, volume 3, 1956.
- [29] H. Kanber, R.J. Cipolli, and W. B. Henderson, "A Comparison of Rapid Thermal Annealing and Controlled Atmosphere Annealing of Si-implanted GaAs," J. Appl. Phys. 57 (10), 15 May 1985.
- [30] J. P. de Souza, D. K. Sadana, H. Baratte, and F. Cardone, "Annealing Behavior of GaAs Implanted with Si⁺ and SiF⁺ and Rapid Thermally Annealed with Plasma-enhanced Chemical Vapor Deposited Silicon Nitride Cap," Appl. Phys. Lett. 57 (11), 10 September 1990.
- [31] A. C. T. Tang, B. J. Scaly, and A. A. Rezazadeh, "Effects of Annealing on Electrical Properties of Se-implanted GaAs," Electronics Letters 20th July 1989, Vol. 25 No. 15.
- [32] M. E. Greiner, "Silicon Diffusion in Gallium Arsenide Using Rapid Thermal Processing," Ph.D. Thesis, Stanford University, Stanford, 1984.
- [33] A. Bindal, K. L. Wang, S. J. Chang, M. A. Kallel, P.K. Chu, "A Process Simulation Model for Silicon Ion Implantation in Undoped, LEC-Grown GaAs," J. Electrochemical Society, 136, 3414, 1989.
- [34] L. S. Vanasupa, "Electrical Activation of Implanted Silicon in Gallium Arsenide," Ph.D. Thesis, Stanford University, Stanford, 1991.
- [35] A. Lidow, J. F. Gibbons, V. R. Deline and C. A. Evens, Jr, "Ion-implanted Se in GaAs," J. Appl. Phys. 51(8), 4130 August 1980.
- [36] J. K. Dhiman and K. L. Wang, "Process Modeling of n-Type Doping in Gallium Arsenide," Journal of Electrochemical Society, Vol. 131, No. 12, 1984.

- [37] Stephen E. Hansen and Michael D. Deal, "Suprem3.5 - A Program for Process and Device Simulation of GaAs," Stanford University, 1990.
- [38] Jong-Lam Lee, Jin Sup Kim, Hyung Moo Park, and Dong Sung Ma, "Depth Profiles on Ion Implantation Induced Vacancy-type Defects in GaAs and Si Observed by Slow Positron," *Appl. Phys. Lett.* 53 (14), 3 pp. 1302, 3 October 1988.
- [39] B.A. Lombos, T. Bretagnon, A. Jean, R. Le Van Mao, S. Bourassa, J. P. Dodelet, "EL2 Trends in As-rich GaAs Grown by Close-spaced Vapor Transport," *J. Appl. Phys.* 67 (4), pp. 1879 15 February 1990.
- [40] Yao-Tsung Tsai and Timothy A. Grotjohn, "Source and Drain Resistance Studies of Short Channel MESFET's Using Two-Dimensional Device Simulators," *IEEE Transactions on Electron Devices*, Vol. 37. No. 3. March 1990.
- [41] P. A. Kirkby, P. R Selway, L. D. Westbrook, "Photoelastic Waveguide and Their Effect on Stripe-Geometry GaAs/Ga_{1-x}Al_xAs Lasers," *J. Appl. Phys.* 50(7), July 1979.
- [42] Peter M. Asbeck, Chien-ping Lee, Mau-chung F. Chang, "Piezoelectric Effects in GaAs FET's and Their Role in Orientation-Dependent Device Characteristics," *IEEE Transactions on Electron Devices*, Vol. ED-31, No. 10, October 1984.
- [43] N. I. Muskhelishvili. "Some Basic Problems of the Mathematical Theory of Elasticity," P. Noordhoff Ltd. 1963.
- [44] J. F. Nye, "Physical Properties of Crystals," Clarendon Press, London 1985.